MNRAS **000**, 1–27 (2017) Preprint 3 August 2017 Compiled using MNRAS LATEX style file v3.0

Supernova Remnants in M33: X-ray Properties as Observed by *XMM-Newton*

Kristen Garofali,[1]⋆ Benjamin F. Williams,[1] Paul P. Plucinsky,[4] Terrance J. Gaetz,[4] Brian Wold,[1] Frank Haberl[2] Knox S. Long,[5] William P. Blair,[3] Thomas G. Pannuti,[6] P. Frank Winkler,[7] Jacob Gross,[1]

[1]*University of Washington Astronomy Department, Box 351580, Seattle, WA, 98195*
[2]*Max-Planck-Institut für extraterrestrische Physik, Giessenbachstraße, 85748 Garching, Germany*
[3]*Department of Physics and Astronomy, Johns Hopkins University, 3400 North Charles Street, Baltimore, MD 21218*
[4]*Harvard-Smithsonian Center for Astrophysics, 60 Garden Street, Cambridge, MA 02138*
[5]*Space Telescope Science Institute, 3700 San Martin Drive, Baltimore, MD 21218*
[6]*Space Science Center, Department of Earth and Space Sciences, 235 Martindale Drive, Morehead State University, Morehead, KY 40351*
[7]*Department of Physics, Middlebury College, Middlebury, VT 05753*

3 August 2017

ABSTRACT

We have carried out a study of the X-ray properties of the supernova remnant (SNR) population in M33 with *XMM-Newton*, comprising deep observations of 8 fields in M33 covering all of the area within the D_{25} contours, and with a typical luminosity of 7.1×10^{34} erg s^{-1} (0.2-2.0 keV) . Here we report our work to characterize the X-ray properties of the previously identified SNRs in M33, as well as our search for new X-ray detected SNRs. With our deep observations and large field of view we have detected 105 SNRs at the 3σ level, of which 54 SNRs are newly detected in X-rays, and three are newly discovered SNRs. Combining *XMM-Newton* data with deep *Chandra* survey data allows detailed spectral fitting of 15 SNRs, for which we have measured temperatures, ionization timescales, and individual abundances. This large sample of SNRs allows us to construct an X-ray luminosity function, and compare its shape to luminosity functions from host galaxies of differing metallicities and star formation rates to look for environmental effects on SNR properties. We conclude that while metallicity may play a role in SNR population characteristics, differing star formation histories on short timescales, and small-scale environmental effects appear to cause more significant differences between X-ray luminosity distributions. In addition, we analyze the X-ray detectability of SNRs, and find that in M33 SNRs with higher [SII]/Hα ratios, as well as those with smaller galactocentric distances, are more detectable in X-rays.

Key words: ISM: supernova remnants, X-rays: supernova remnants, Astronomical Data bases: catalogues, Galaxies: Local Group

1 INTRODUCTION

Supernova remnants (SNRs) deposit energy and metals into the interstellar medium (ISM), and thus are key drivers of galactic chemical evolution. The ejecta and shock wave from the supernova (SN) explosion interact with the ISM, making it visible in optical, radio and X-ray wavelengths. The supernova events themselves are short-lived, so very few are available to study nearby in detail. The SNRs they leave behind, by contrast, offer a way to unlock information about the progenitor and its lasting impacts on the ISM. Typically, thermal X-ray spectra have been used to infer properties of the young, ejecta-dominated SNRs that are indicative of the supernova progenitor, and therefore significant effort has been put into X-ray detections (e.g. Vink et al. 2003; Badenes et al. 2003; Gaetz et al. 2007; Badenes et al. 2007; Reynolds 2008; Long et al. 2010; Vink 2012; Yamaguchi et al. 2014; Pannuti et al. 2014; Long et al. 2014; Maggi et al. 2016).

It is difficult to systematically compare SNR properties, such as progenitor type, with their effect on the ISM, because most SNR studies in the Milky Way to date have focused on individual SNRs. In addition, SNR population studies in the Milky Way are difficult due to distance uncertainties and variable absorption to the individual objects (Woltjer 1972; Milne 1979; Raymond 1984; Green 2014). SNRs in Local Group galaxies, however, are in the unique position

⋆ E-mail: garofali@uw.edu (KG)

to be studied as a population in relation to the surrounding stellar population and ISM, because they are all at a common distance and have similar foreground extinction. In the Magellenic Clouds, the progenitor types, spectral properties, X-ray morphologies, explosion types and size distribution of the SNR population have all been well characterized in optical, X-ray, and radio wavelengths (Mathewson & Clarke 1973; Long & Helfand 1979; Mathewson et al. 1983; Chu & Kennicutt 1988; Hughes et al. 1998; Badenes et al. 2010; Lopez et al. 2011; Maggi et al. 2016, 2014). M31 hosts a population of optically identified SNRs (Blair et al. 1981; Braun & Walterbos 1993; Magnier et al. 1995; Lee & Lee 2014a) for which progenitor masses have been estimated (Jennings et al. 2012, 2014), and X-ray measurements have been made with *XMM-Newton* (Sasaki et al. 2012). Outside the Local Group, populations of extragalactic SNRs have been identified in nearby spiral galaxies in the optical, based on emission-line ratios (Matonick & Fesen 1997; Blair et al. 2012; Leonidaki et al. 2013), X-ray emission (Pannuti et al. 2007; Leonidaki et al. 2010), and based on radio observations (Lacey & Duric 2001; Pannuti et al. 2002).

M33 has perhaps the best-characterized SNR population of any spiral galaxy (Sabbadin 1979; Dodorico et al. 1980; Gordon et al. 1998; Long et al. 2010; Sarbadhicary et al. 2017), making it a prime target to extend these previous works characterizing extragalactic SNRs. In particular, M33, a late-type Sc spiral, is well-suited for X-ray studies of SNRs because of its proximity to the Milky Way at 817±58 kpc (Freedman et al. 2001), its close to face-on angle of inclination, $i = 56° \pm 1°$ (Zaritsky et al. 1989), and its low foreground absorption ($N_H \approx 6\times10^{20}$cm^{-2}, Stark et al. 1992). Previous detailed multi-wavelength surveys have revealed a rich SNR population (218 candidates, 86 confirmed via multi-wavelength detections) in optical, radio, and X-ray wavelengths. Using optical emission-line ratios Gordon et al. (1998) identified a population of 98 SNR candidates in M33. Recently, Long et al. (2010, hereafter L10) carried out a multiwavelength study of 131 of the previously known 137 SNRs in the galaxy; they detected 82 (58) at the 2σ (3σ) level with *Chandra*, and obtained upper limits for the rest. Most recently, Lee & Lee (2014b, hereafter LL14) boosted the number to 199 optically selected SNR candidates, of which 78 were not previously reported in L10's catalog. Here we carry out an analysis of the properties of all 218 known and suggested SNRs in M33. This includes the 137 sources described by L10 (of which 121 overlap with the sources discussed by LL14), the 78 new sources identified as candidates by LL14, and 3 X-ray candidates identified by Williams et al. (2015, hereafter W15).

Herein we utilize data from a deep survey of M33 using an 8 field *XMM-Newton* mosaic that extends out to the D_{25} isophote. The point source catalog from this survey was published by W15. In this paper, we leverage both the excellent soft sensitivity of *XMM-Newton*, as well as the large field-of-view from the W15 survey as they pertain to the SNR population in M33. With this *XMM-Newton* survey, all 218 SNR candidates are within the field-of-view and refinements can be made to the properties of those SNRs already detected at X-ray and/or optical wavelengths. For the purposes of obtaining X-ray spectral fits we have also made use of *Chandra* ACIS Survey of M33 (ChASeM33, Tüllmann et al. 2011) data where possible. In section 2, we describe the data used from this and previous surveys as well as the data reprocessing and reduction techniques. Section 3 outlines the SNR catalog, and details the characterization of the SNR population based on spectral fitting, hardness ratios (HRs), and X-ray morphology. In Section 4 we discuss the results from this most recent X-ray survey of the M33 SNR population, including the shape of the X-ray luminosity function, and the implications for SNR detectability, and finally in Section 5 we present our conclusions.

2 SURVEY OVERVIEW

The observations and analysis of the *XMM-Newton* survey data of M33 used in this paper are described by W15. The W15 survey consists of an 8 field *XMM-Newton* mosaic of M33 with a summed exposure time of 900 ks extending out to the D_{25} isophote and to a limiting 0.2-4.5 keV luminosity of 4×10^{34} erg s^{-1} at the distance of M33. For the purpose of analyzing the SNR population, we have optimized our reduction of the survey data for extended sources, as we describe in Section 2.1 and in the Appendix. All 218 previously identified SNR candidates are within the field-of-view of W15, allowing for cross-correlation of the W15 X-ray catalog with both the existing X-ray and optical catalogs of L10 and LL14, as well as identification of 3 new X-ray selected SNRs (described in Section 3.1) based on X-ray HRs and visual inspection of Local Group Galaxy Survey (LGGS) data (Massey et al. 2006). The positions for all sources used in the remainder of this analysis come from the catalog of W15. The X-ray fluxes, and HRs reported in Table **??** and Table **??** come from custom measurements at the positions of all 218 SNR candidates using the *XMM-Newton* data in the bands described in Section 2.1. The *XMM-Newton* spectra used in the spectral fitting described in Section 3.2 were extracted specifically for this analysis as described in the Appendix.

In addition to the catalog of W15, we utilize high resolution observations from the *Chandra* ACIS Survey of M33 (ChASeM33, Tüllmann et al. 2011), which had a total exposure time of 1.4 Ms and covered about 70% of the D_{25} isophote down to a limiting 0.35-8.0 keV luminosity of 2.4×10^{34} ergs s^{-1}. The SNR catalog from the ChASeM33 survey is described in L10, and, in addition to cross-correlating our SNR candidates with those of L10, we also use their `ACIS` spectra when available for spectral fits.

We also cross-correlate our sources with the optically selected SNR candidate catalog of LL14. Their survey used narrow-band images from the LGGS (Massey et al. 2006) to identify SNR candidates based on emission-line ratios ([SII]/Hα > 0.4) and shell-like or circular morphology for sources smaller than 100 pc. The L10 survey, by contrast, did not initially cut candidates based on morphological or size considerations, focusing instead on evidence of shock-heating, and further used only portions of the LGGS within the *Chandra* footprint. For the purposes of this paper, we have kept all objects contained in both survey lists. We discuss our measurements at the locations of all sources in each catalog in Section 3.1.

In addition to finding SNR candidates, LL14 assign each candidate in their catalog a tentative progenitor classification of core-collapse (CC) or Type Ia based upon the surrounding stellar population. CC SNe result from the explosion of a massive star and thus are expected to be in regions of recent star formation nearby other OB stars. Type Ia, or thermonuclear, SNe are caused by the detonation of a white dwarf (WD) that has reached its Chandrasekhar limit and are expected in regions of little to no recent star formation (i.e. few nearby OB stars). However, it is possible a Type Ia SN could occur near a region of OB stars in areas with multiple epochs of star formation, highlighting the need for a full star formation history of the surrounding region to determine more reliably the progenitor class. Such classifications exist for a handful of SNRs in M33 from the work of Jennings et al. (2014). These SNR progenitor classifications are the result of measured progenitor masses from detailed star formation histories of the stellar populations surrounding each

SNR, and are considered robust determinations. When the classifications from Jennings et al. (2014) are unavailable, we instead use the LL14 tentative progenitor type labels. Together these classifications are used to explore the efficacy of measured HRs (Section 3.4) in typing SNR progenitors.

2.1 Reprocessing of *XMM-Newton* Data

While the vast majority of the reduction techniques for the analysis presented here was described in detail in W15, there were some special considerations that we employed for source detection and background characterization when looking specifically for the SNRs in M33, which slightly differ from the description in W15.

For detecting and measuring extended sources, it is beneficial to use the software provided by the `Extended Source Analysis Software (ESAS)` (Kuntz & Snowden 2008), a package within `SAS` optimized for extended sources, which models the background light curves during an observation and identifies time periods when the background level is significantly enhanced compared to the quiescent background, allowing cleaner separation of extended sources from the background as well as spectra with less background contamination.

We selected good-time intervals (GTIs) using the `ESAS` tools `pn-filter` and `mos-filter`. Utilizing the unexposed corner sections of the CCDs, count thresholds are chosen by fitting a Gaussian peak at the quiescent count rate. A GTI file is produced which includes only time intervals where the count rate was within 2σ of the peak of the aforementioned Gaussian. Within the `ESAS` package `pn-filter` and `mos-filter` were applied to the `SAS` task `espfilt` to determine the GTIs. We then applied these GTIs to our event lists for spectral extraction. Our spectral extraction required a large amount of customization. We therefore place a detailed explanation in the Appendix. The extracted spectra are used for the spectral fitting described in 3.2.2.

When searching for soft and extended gas emission sources (such as large SNRs or HII regions), we applied the same `emosaicprep` and `emosaicproc` tasks as for the point sources, but using the `ESAS`-processed event lists. For the purposes of detecting SNRs, the energy range was set to 0.2-2.0 keV and the positions of the L10 and LL14 SNR candidates were input into `emldetect`. For the 0.2-2.0 keV band we ran `emldetect` simultaneously on the 0.2-0.5 keV, 0.5-1.0 keV, and 1.0-2.0 keV bands, and let `emldetect` calculate the full band (0.2-2.0 keV) totals based on the provided exposure times, background images, and masks. This energy range was chosen to leverage the soft sensitivity of *XMM-Newton* for SNR detection. The pn requires more conservative flagging be applied to the event list in the softest band (0.2-0.5 keV) to avoid spurious detections. For this reason, the individual bands were run separately with flagging as described in W15, and then combined to create a full band (0.2-2.0 keV). For the purposes of measuring and comparing luminosities, the energy range was also set to 0.35-2.0 keV to match the band of L10. These measurements at the locations of previously known SNRs are discussed in 3.1.

Another critical adjustment to make was the choice of energy conversion factor (ECF) values. The list of source positions from `emosaicproc` was fed to `emldetect` to calculate on-axis equivalent count rates and convert these values to a flux using ECFs selected during the detection script. Table 1 lists the ECFs used to calculate the fluxes in the 0.2-2.0 keV band (plus component bands) which was used for source detection, and the 0.35-2.0 keV band which was used for comparison to L10, and the 0.3-0.7 keV, 0.7-1.1. keV, and 1.1-4.2 keV bands, which were used for HR calculations in Section 3.4. The unabsorbed ECFs were calculated based on `XSPEC` simulations of an `apec` spectrum with absorption with parameters N_H=1x10^{21} cm^{-2}, kT = 0.6 keV, and elemental abundance set to half solar. This spectrum was also chosen to remain consistent with L10. Futhermore, we ensured that the locations of all SNR candidates were included in the candidate source list that was measured by the `emldetect` step of our analysis routine. Thus, we were able to obtain either detections or upper limits for all SNR candidates. Occasionally, `emldetect` fails to properly combine the individual bands to produce a reliable full band total. In these cases (8% of sources), the source counts in the full band (0.2-2.0 keV) are a factor of 2 discrepant from the sum total of the individual bands (0.2-0.5 keV, 0.5-1.0 keV, and 1.0-2.0 keV). We denote these sources with a 't' flag in Table **??** and Table **??**. These sources still have reliable measurements in the individual bands, so for their full band 0.2-2.0 keV totals we report the counts, count rate, and flux values as the sum of the individual bands. For all other sources the total flux values are output from `emldetect` and represent the sum of the fluxes from each EPIC instrument weighted by the appropriate calibration files. All sources are listed in Table **??**.

Table 1. Unabsorbed energy correction factors (ECFs) for the bands and instruments used in this survey. ECF units are counts erg cm^{-2}.

Energy Band (keV)	pn	MOS1	MOS2
0.35-2.0	1.8×10^{-12}	7.45×10^{-12}	7.44×10^{-12}
0.2-2.0	2.5×10^{-12}	8.2×10^{-12}	8.1×10^{-12}
0.2-0.5	4.2×10^{-12}	2.7×10^{-11}	2.8×10^{-11}
0.5-1.0	1.8×10^{-12}	7.8×10^{-12}	7.8×10^{-11}
1.0-2.0	1.9×10^{-12}	5.9×10^{-12}	5.8×10^{-12}
0.3-0.7	1.8×10^{-12}	1.1×10^{-11}	1.1×10^{-11}
0.7-1.1	1.9×10^{-12}	7.8×10^{-12}	7.7×10^{-12}
1.1-4.2	2.0×10^{-12}	6.1×10^{-12}	6.1×10^{-12}

3 RESULTS

Our goal is to provide the best possible characterization of the SNR population of M33 given all of the available data. Because *XMM-Newton* provides high soft-band sensitivity, this new survey provides further constraints on SNR spectral fits and HR measures which can potentially be used to constrain progenitor explosion type. We describe the sample of SNRs measured in this survey, as well as each of these methods as applied to that sample below.

3.1 Catalog of M33 SNRs

To measure fluxes or, where not possible, establish upper limits on the flux of SNRs in M33, we measured the locations of SNR candidates from L10, LL14, and W15 (218 total sources) in both the 0.2-2.0 keV band as well as the 0.35-2.0 keV band to be consistent with L10. We find that the average signal-to-noise is higher in the 0.2-2.0 keV band, and after verifying all measurements by eye to remove spurious detections in both bands, we found that using the 0.2-2.0 keV band results in 12 more 3σ detections than using the 0.35-2.0 keV band. We therefore conclude that the 0.2-2.0 keV band is better for detection of SNRs when using *XMM-Newton* and that only 3σ measurements should be taken as reliable detections, as there can be fluctuations in the background

Table 2: All 218 SNR and SNR candidates in our sample. Columns 1-3: ID number from this catalog, ID number in L10, and ID number in LL14. Columns 4-5: source RA and Dec from this catalog. Columns 6-7: source counts and associated errors, and count rates and associated errors in the 0.2-2.0 keV band (used for detection). Columns 8-9: fluxes in the 0.2-2.0 keV band (used for detection), and fluxes in the 0.35-2.0 keV band (used for comparison to L10). Columns 10-11: optical SNR sizes from the L10 and LL14 catalogs. Columns 12-13: [SII]/Hα ratio from the L10 and LL14 catalogs (used for optical selection of candidates). Columns 14-15: log of the Hα luminosity from the L10 and LL14 catalogs. All units are given in the column headers.

ID	L10	LL14	RA	Dec	0.2-2.0 Cts	0.2-2.0 Ct Rate (s^{-1})	0.2-2.0 Flux (ergs cm^{-2} s^{-1})	0.35-2.0 Flux (ergs cm^{-2} s^{-1})	D(pc) L10	D(pc) LL14	[SII]/Hα L10	[SII]/Hα LL14	log(L(Hα) (ergs s^{-1})) L10	log(L(Hα) (ergs s^{-1})) LL14
XMM-001	–	1	1:32:25.78	30:30:04.03	21 ± 11	2.34e-04 ± 1.30e-04	<8.20e-16	<2.18e-16	–	81.0	–	0.74	–	36.16
XMM-002	–	2	1:32:27.85	30:35:44.58	25 ± 15	2.81e-04 ± 1.80e-04	<6.77e-16	<3.44e-16	–	72.0	–	0.98	–	36.05
XMM-003	1	–	1:32:30.83	30:27:45.99	107 ± 19	1.15e-03 ± 2.09e-04	1.40e-15	1.12e-15	123.0	–	0.77	–	36.98	–
XMM-004	2	3	1:32:31.41	30:35:32.90	66 ± 19	7.76e-04 ± 2.49e-04	1.09e-15	8.62e-16	29.0	28.0	0.44	0.59	36.20	36.02
XMM-005	–	4	1:32:35.36	30:35:19.81	27 ± 14	2.82e-04 ± 1.51e-04	<7.61e-16	<2.23e-16	–	85.0	–	0.50	–	36.36
XMM-006	–	5	1:32:37.36	30:18:03.10	296 ± 23	6.02e-03 ± 4.93e-04	8.49e-15	7.30e-15	–	85.0	–	0.60	–	36.15
XMM-007	–	6	1:32:39.78	30:27:54.95	11 ± 13	1.07e-04 ± 1.19e-04	<3.59e-16	<1.76e-16	–	36.0	–	0.93	–	35.36
XMM-008	–	7	1:32:40.23	30:16:21.24	4 ± 7	1.16e-04 ± 2.16e-04	<5.33e-16	<2.85e-16	–	44.0	–	0.52	–	35.65
XMM-009	–	8	1:32:40.53	30:16:37.20	74 ± 13	1.89e-03 ± 3.53e-04	1.76e-15	2.03e-15	–	42.0	–	0.79	–	35.36
XMM-010	–	9	1:32:40.94	30:31:51.05	39 ± 16	3.15e-04 ± 1.33e-04	7.98e-16	<3.35e-16	–	86.0	–	0.51	–	36.36
XMM-011	3	–	1:32:42.54	30:20:58.83	10 ± 10	1.22e-04 ± 1.33e-04	<5.59e-16	<1.31e-16	100.0	–	0.55	–	36.90	–
XMM-012[n]	–	10	1:32:42.71	30:36:20.06	51 ± 16	5.63e-04 ± 1.81e-04	<1.42e-15	2.85e-16	–	58.0	–	0.49	–	36.07
XMM-013[n]	4	11	1:32:44.83	30:22:14.54	47 ± 15	5.54e-04 ± 1.86e-04	<1.57e-15	4.93e-16	39.0	38.0	–	0.85	35.97	35.94
XMM-014[n]	–	12	1:32:45.47	30:23:14.15	15 ± 12	1.89e-04 ± 1.45e-04	<5.99e-16	<3.23e-16	–	45.0	–	0.59	–	35.84
XMM-015	5	13	1:32:46.61	30:34:37.00	253 ± 26	2.45e-03 ± 2.60e-04	4.89e-15	2.39e-15	45.0	42.0	0.78	0.89	36.08	35.97
XMM-016	–	14	1:32:51.84	30:51:08.98	19 ± 10	4.65e-04 ± 2.70e-04	<9.87e-16	1.03e-15	–	40.0	–	0.72	–	35.34
XMM-017[c]	6	15	1:32:52.76	30:38:12.57	55 ± 42	5.58e-04 ± 4.40e-04	<1.45e-15	<6.62e-16	56.0	56.0	0.55	0.57	36.38	36.28
XMM-018	–	16	1:32:52.80	30:31:34.23	15 ± 13	1.22e-04 ± 1.26e-04	<5.49e-16	<1.09e-16	–	68.0	–	0.56	–	36.37
XMM-019	7	18	1:32:53.36	30:48:23.06	53 ± 15	1.15e-03 ± 3.29e-04	1.61e-15	1.49e-15	73.0	56.0	–	0.81	35.88	35.78
XMM-020[x]	8	17	1:32:53.40	30:37:56.95	79 ± 31	8.88e-04 ± 3.54e-04	<1.23e-15	<6.10e-16	51.0	50.0	0.61	0.60	36.65	36.58
XMM-021	9	19	1:32:54.10	30:25:31.79	43 ± 19	4.37e-04 ± 2.43e-04	9.14e-16	<4.07e-16	39.0	42.0	–	0.81	36.18	36.15
XMM-022	10	21	1:32:55.96	30:40:33.57	134 ± 23	1.51e-03 ± 2.66e-04	2.68e-15	1.61e-15	93.0	96.0	0.81	0.87	36.83	36.79
XMM-023	–	20	1:32:56.12	30:33:30.44	68 ± 20	5.57e-04 ± 1.76e-04	8.14e-16	5.88e-16	–	80.0	–	0.85	–	36.30
XMM-024	11	22	1:32:57.10	30:39:25.87	474 ± 32	5.31e-03 ± 3.61e-04	8.80e-15	6.00e-15	20.0	22.0	0.84	0.83	36.46	36.42
XMM-025	–	23	1:32:57.18	30:39:14.69	31 ± 17	3.48e-04 ± 1.94e-04	<9.35e-16	<2.99e-16	–	37.0	–	0.47	–	35.93
XMM-026[t]	12	–	1:33:00.15	30:30:46.18	52 ± 41	3.96e-04 ± 3.17e-04	4.52e-16	<3.28e-16	52.0	–	–	–	37.43	–
XMM-027	13	24	1:33:00.40	30:44:07.57	407 ± 33	4.20e-03 ± 3.49e-04	6.37e-15	4.44e-15	33.0	34.0	0.47	0.56	35.72	35.73
XMM-028	14	25	1:33:00.67	30:30:59.28	31 ± 19	2.34e-04 ± 1.51e-04	<4.86e-16	<2.46e-16	46.0	46.0	–	0.56	37.20	37.21
XMM-029	15	26	1:33:01.51	30:30:49.59	45 ± 23	3.47e-04 ± 1.85e-04	<9.16e-16	<4.75e-16	28.0	26.0	–	0.54	36.32	36.43
XMM-030	16	27	1:33:02.93	30:32:29.65	93 ± 20	7.93e-04 ± 1.85e-04	1.04e-15	6.11e-16	51.0	49.0	0.97	0.74	36.40	36.34
XMM-031	17	28	1:33:03.58	30:31:18.27	225 ± 27	1.70e-03 ± 2.11e-04	3.15e-15	1.73e-15	33.0	34.0	1.07	1.10	36.15	36.11
XMM-032	18	29	1:33:04.07	30:39:51.65	217 ± 27	2.30e-03 ± 2.92e-04	3.07e-15	2.97e-15	30.0	33.0	0.49	0.66	36.64	36.62
XMM-033	19	–	1:33:07.55	30:42:52.51	71 ± 23	6.61e-04 ± 2.10e-04	1.22e-15	7.08e-16	71.0	–	–	–	36.82	–
XMM-034	–	30	1:33:08.77	30:12:15.64	928 ± 36	2.50e-02 ± 9.76e-04	4.28e-14	2.77e-14	–	27.0	–	0.60	–	35.60
XMM-035	20	31	1:33:08.93	30:26:57.31	181 ± 26	1.52e-03 ± 2.35e-04	2.21e-15	1.46e-15	51.0	50.0	–	0.79	36.26	36.22
XMM-036	–	32	1:33:09.69	30:16:39.01	21 ± 9	4.11e-04 ± 1.75e-04	7.12e-16	<3.27e-16	–	85.0	–	1.15	–	35.88
XMM-037	21	33	1:33:09.87	30:39:34.85	39 ± 22	4.25e-04 ± 2.35e-04	<8.31e-16	<5.73e-16	67.0	100.0	0.66	0.51	36.58	36.97
XMM-038	22	34	1:33:10.16	30:42:22.26	372 ± 35	3.61e-03 ± 3.45e-04	6.64e-15	3.95e-15	27.0	24.0	0.86	0.85	35.78	35.65
XMM-039	23	35	1:33:11.16	30:39:43.41	1807 ± 56	1.68e-02 ± 5.64e-04	2.88e-14	1.82e-14	25.0	24.0	0.78	0.68	35.93	36.00
XMM-040	24	36	1:33:11.28	30:34:23.46	15 ± 14	1.64e-04 ± 1.69e-04	<4.64e-16	<4.23e-16	99.0	92.0	0.49	0.45	37.08	37.05
XMM-041	25	37	1:33:11.80	30:38:40.48	21032 ± 190	1.89e-01 ± 1.76e-03	2.82e-13	2.18e-13	25.0	18.0	0.55	0.49	36.30	36.09
XMM-042	–	38	1:33:13.46	30:28:13.12	99 ± 22	7.04e-04 ± 1.58e-04	9.98e-16	6.20e-16	–	74.0	–	0.54	–	36.33

ID	L10	LL14	RA	Dec	0.2-2.0 Cts	0.2-2.0 Ct Rate (s^{-1})	0.2-2.0 Flux ergs s cm^{-2}	0.35-2.0 Flux ergs s cm^{-2}	D(pc) L10	D(pc) LL14	[SII]/Hα L10	[SII]/Hα LL14	log(L(Hα) (ergs s^{-1})) L10	log(L(Hα) (ergs s^{-1})) LL14
XMM-043	–	39	1:33:13.81	30:39:44.01	31 ± 20	2.89e-04 ± 1.95e-04	<7.41e-16	<4.31e-16	–	65.0	–	0.51	–	36.28
XMM-044	–	40	1:33:15.35	30:35:41.97	22 ± 18	2.12e-04 ± 1.68e-04	<4.84e-16	<2.51e-16	–	75.0	–	0.74	–	35.95
XMM-045	26	41	1:33:16.73	30:46:10.25	36 ± 17	4.70e-04 ± 2.45e-04	1.33e-15	9.01e-16	73.0	70.0	–	0.62	36.72	36.63
XMM-046	27	42	1:33:17.44	30:31:28.50	79 ± 22	5.17e-04 ± 1.46e-04	8.07e-16	5.74e-16	44.0	34.0	0.91	0.81	36.00	36.07
XMM-047	–	43	1:33:17.55	30:46:45.64	58 ± 19	6.50e-04 ± 2.23e-04	1.15e-15	9.53e-16	–	68.0	–	0.60	–	36.39
XMM-048	–	44	1:33:18.13	30:33:38.67	27 ± 15	2.17e-04 ± 1.26e-04	<6.57e-16	<2.53e-16	–	30.0	–	0.47	–	35.45
XMM-049	28	–	1:33:18.80	30:27:04.38	22 ± 17	1.67e-04 ± 1.23e-04	<4.60e-16	<1.63e-16	179.0	–	–	–	37.18	–
XMM-050	29	45	1:33:18.94	30:46:51.88	92 ± 19	1.21e-03 ± 2.55e-04	2.12e-15	7.01e-16	66.0	66.0	–	1.02	36.20	36.22
XMM-051	–	46	1:33:19.52	30:12:29.22	13 ± 8	3.57e-04 ± 2.08e-04	<7.96e-16	<3.80e-16	–	69.0	–	0.69	–	35.81
XMM-052	–	47	1:33:20.76	30:25:55.21	42 ± 18	2.75e-04 ± 1.24e-04	7.28e-16	<1.90e-16	–	16.0	–	0.46	–	35.27
XMM-053	–	48	1:33:21.19	30:19:20.61	35 ± 15	3.72e-04 ± 1.63e-04	9.76e-16	<3.18e-16	–	74.0	–	0.55	–	36.01
XMM-054[t]	–	49	1:33:21.33	30:30:31.63	1036 ± 341	6.54e-03 ± 2.18e-03	6.95e-15	5.19e-16	–	55.0	–	0.42	–	36.25
XMM-055[n]	30	50	1:33:21.64	30:31:31.09	79 ± 43	5.34e-04 ± 2.98e-04	6.12e-16	<4.80e-16	76.0	80.0	–	0.46	36.67	36.76
XMM-056	–	51	1:33:21.94	30:25:58.36	49 ± 19	3.15e-04 ± 1.23e-04	6.86e-16	<2.71e-16	–	36.0	–	0.51	–	36.05
XMM-057	31	52	1:33:22.67	30:27:04.00	87 ± 24	6.07e-04 ± 1.67e-04	8.09e-16	4.31e-16	20.0	20.0	0.95	1.00	35.84	35.78
XMM-058	32	53	1:33:23.85	30:26:13.53	66 ± 27	4.28e-04 ± 1.81e-04	7.63e-16	<5.65e-16	21.0	24.0	1.06	1.12	36.26	36.24
XMM-059	–	54	1:33:24.01	30:36:56.81	72 ± 21	6.53e-04 ± 1.96e-04	8.79e-16	6.35e-16	–	76.0	–	0.64	–	36.20
XMM-060	–	55	1:33:24.18	30:28:50.24	66 ± 22	4.10e-04 ± 1.39e-04	1.18e-15	<4.29e-16	–	50.0	–	1.05	–	35.69
XMM-061	33	56	1:33:27.07	30:47:48.65	36 ± 15	3.82e-04 ± 1.74e-04	1.10e-15	<3.84e-16	67.0	62.0	0.57	0.81	36.38	36.35
XMM-062	–	57	1:33:27.32	30:23:59.34	33 ± 16	2.49e-04 ± 1.28e-04	6.92e-16	<2.76e-16	–	34.0	–	0.48	–	35.60
XMM-063[n]	–	58	1:33:27.92	30:18:17.35	45 ± 14	5.70e-04 ± 1.90e-04	<9.07e-16	7.13e-16	–	40.0	–	0.93	–	35.69
XMM-064	–	59	1:33:28.00	30:16:01.14	10 ± 9	1.42e-04 ± 1.33e-04	<5.46e-16	<1.19e-16	–	37.0	–	0.81	–	35.28
XMM-065	34	60	1:33:28.11	30:31:33.53	749 ± 42	4.48e-03 ± 2.55e-04	7.23e-15	5.28e-15	32.0	32.0	0.55	0.55	36.38	36.31
XMM-066	35	–	1:33:28.92	30:47:43.95	736 ± 36	8.50e-03 ± 4.26e-04	1.50e-14	8.86e-15	19.0	–	0.36	–	35.76	–
XMM-067	36	61	1:33:29.08	30:42:15.99	3706 ± 78	3.29e-02 ± 7.08e-04	5.13e-14	3.88e-14	18.0	21.0	1.13	0.95	36.81	36.80
XMM-068	37	62	1:33:29.48	30:49:10.63	2170 ± 59	2.42e-02 ± 6.53e-04	4.04e-14	2.69e-14	32.0	31.0	0.75	0.78	35.86	35.81
XMM-069	–	63	1:33:29.79	31:01:53.00	52 ± 14	8.92e-04 ± 2.44e-04	3.78e-15	1.33e-15	–	47.0	–	0.79	–	35.71
XMM-070	38	64	1:33:30.21	30:47:43.83	27 ± 15	2.88e-04 ± 1.67e-04	<6.37e-16	<4.36e-16	51.0	40.0	0.31	0.45	36.43	36.26
XMM-071	–	65	1:33:30.64	30:21:01.49	57 ± 19	6.14e-04 ± 2.10e-04	1.63e-15	7.61e-16	–	88.0	–	0.79	–	36.40
XMM-072[n]	–	66	1:33:31.20	30:21:14.25	65 ± 19	6.39e-04 ± 1.91e-04	<1.35e-15	9.02e-16	–	58.0	–	0.78	–	36.09
XMM-073	39	67	1:33:31.30	30:33:32.42	7361 ± 106	5.16e-02 ± 7.56e-04	7.95e-14	6.00e-14	13.0	44.0	0.95	0.68	36.98	37.17
XMM-074	40	68	1:33:31.34	30:42:18.33	95 ± 27	8.40e-04 ± 2.34e-04	1.12e-15	1.05e-15	55.0	52.0	0.65	0.40	36.45	36.43
XMM-075	41	69	1:33:32.17	30:31:02.62	172 ± 30	1.04e-03 ± 1.81e-04	1.47e-15	1.28e-15	97.0	82.0	–	1.02	36.23	36.30
XMM-076	–	72	1:33:34.99	30:29:54.55	134 ± 26	8.38e-04 ± 1.61e-04	1.35e-15	6.54e-16	–	18.0	–	0.93	–	35.93
XMM-077	–	70	1:33:35.10	30:19:24.16	31 ± 15	3.38e-04 ± 1.65e-04	8.11e-16	<3.56e-16	–	63.0	–	0.81	–	35.78
XMM-078	42	71	1:33:35.14	30:23:07.44	96 ± 20	7.70e-04 ± 1.61e-04	9.27e-16	8.98e-16	43.0	42.0	–	1.51	35.98	35.47
XMM-079[t]	43	–	1:33:35.59	30:42:29.14	276 ± 56	2.49e-03 ± 5.10e-04	2.90e-15	5.45e-15	85.0	–	–	–	36.66	–
XMM-080	44	73	1:33:35.61	30:49:22.96	65 ± 18	7.11e-04 ± 1.98e-04	1.02e-15	7.51e-16	29.0	31.0	1.01	1.05	36.04	36.02
XMM-081[t]	–	–	1:33:35.81	30:31:13.67	322 ± 68	2.38e-03 ± 5.05e-04	2.54e-15	5.08e-15	–	–	–	–	–	–
XMM-082	45	74	1:33:35.97	30:36:26.68	1746 ± 56	1.43e-02 ± 4.73e-04	2.20e-14	1.73e-14	30.0	40.0	0.82	0.69	37.30	37.30
XMM-083[t]	46	76	1:33:36.92	30:32:54.24	3016 ± 531	2.19e-02 ± 3.79e-03	2.57e-14	6.86e-15	39.0	38.0	1.01	1.12	36.11	36.12
XMM-084	–	75	1:33:37.02	30:33:10.04	100 ± 27	6.78e-04 ± 1.88e-04	1.15e-15	7.27e-16	–	74.0	–	0.62	–	36.63
XMM-085	47	77	1:33:37.68	30:40:09.50	234 ± 30	2.01e-03 ± 2.58e-04	2.93e-15	2.63e-15	50.0	50.0	1.11	0.83	36.04	36.13
XMM-086	48	78	1:33:38.01	30:42:18.24	49 ± 21	5.34e-04 ± 2.12e-04	1.04e-15	<3.52e-16	21.0	27.0	0.66	0.57	35.99	36.10
XMM-087	–	79	1:33:38.65	31:02:38.78	25 ± 12	6.25e-04 ± 3.28e-04	1.63e-15	<7.02e-16	–	59.0	–	0.87	–	36.20
XMM-088	–	80	1:33:39.59	30:34:26.02	126 ± 28	8.35e-04 ± 1.93e-04	1.72e-15	3.75e-16	–	61.0	–	0.79	–	36.06
XMM-089	–	–	1:33:39.80	30:31:19.05	243 ± 30	1.99e-03 ± 2.64e-04	3.29e-15	2.15e-15	–	–	–	–	–	–

ID	L10	LL14	RA	Dec	0.2-2.0 Cts	0.2-2.0 Ct Rate (s^{-1})	0.2-2.0 Flux ergs s cm^{-2}	0.35-2.0 Flux ergs s cm^{-2}	D(pc) L10	D(pc) LL14	[SII]/Hα L10	[SII]/Hα LL14	log(L(Hα) (ergs s^{-1})) L10	log(L(Hα) (ergs s^{-1})) LL14
XMM-090	–	81	1:33:40.54	30:10:48.35	138 ± 17	5.39e-03 ± 6.81e-04	8.92e-15	5.41e-15	–	46.0	–	0.76	–	35.97
XMM-091[t]	49	82	1:33:40.66	30:39:40.85	67 ± 40	6.19e-04 ± 3.74e-04	6.67e-16	<1.60e-16	43.0	42.0	–	0.74	36.15	36.27
XMM-092	50	–	1:33:40.73	30:42:35.67	61 ± 22	6.32e-04 ± 2.33e-04	1.26e-15	6.84e-16	71.0	–	0.61	–	36.75	–
XMM-093	51	83	1:33:40.87	30:52:13.75	26 ± 13	2.69e-04 ± 1.67e-04	<7.77e-16	<2.13e-16	60.0	60.0	0.69	0.98	36.18	36.09
XMM-094	52	84	1:33:41.30	30:32:28.45	74 ± 32	4.91e-04 ± 2.09e-04	1.14e-15	<4.77e-16	33.0	40.0	–	0.51	35.95	35.96
XMM-095	–	–	1:33:41.44	30:42:20.77	696 ± 59	7.04e-03 ± 6.03e-04	1.17e-14	8.08e-15	–	–	–	–	–	–
XMM-096	53	85	1:33:41.71	30:21:04.10	7 ± 18	7.25e-05 ± 1.82e-04	<4.15e-16	<1.80e-16	34.0	36.0	0.44	0.62	36.71	36.68
XMM-097	54	86	1:33:42.24	30:20:57.75	24 ± 22	2.24e-04 ± 2.14e-04	<6.65e-16	<2.99e-16	45.0	44.0	–	0.83	36.52	36.49
XMM-098	55	87	1:33:42.91	30:41:49.51	110 ± 25	1.01e-03 ± 2.32e-04	1.34e-15	1.03e-15	44.0	74.0	–	0.50	36.08	36.74
XMM-099	56	88	1:33:43.49	30:41:03.76	61 ± 22	7.49e-04 ± 3.05e-04	1.82e-15	1.10e-15	23.0	26.0	0.89	0.78	35.92	35.99
XMM-100[t]	57	89	1:33:43.70	30:36:11.50	955 ± 161	6.42e-03 ± 1.07e-03	8.37e-15	1.11e-14	36.0	36.0	0.54	0.52	36.08	36.26
XMM-101	58	90	1:33:45.26	30:32:20.09	62 ± 23	4.88e-04 ± 1.76e-04	1.00e-15	<4.80e-16	67.0	70.0	–	0.54	36.86	36.88
XMM-102[c]	59	91	1:33:47.46	30:39:44.74	634 ± 74	6.07e-03 ± 7.15e-04	<6.88e-15	<1.65e-15	42.0	42.0	–	0.74	36.08	36.11
XMM-103[n]	–	92	1:33:47.52	30:17:13.75	57 ± 16	7.59e-04 ± 2.20e-04	<1.03e-15	7.80e-16	–	56.0	–	0.54	–	35.91
XMM-104	–	93	1:33:47.82	30:18:02.09	26 ± 15	3.40e-04 ± 2.04e-04	<9.04e-16	<3.23e-16	–	94.0	–	0.62	–	36.57
XMM-105	–	94	1:33:48.13	30:17:25.87	25 ± 12	3.30e-04 ± 1.62e-04	7.96e-16	<1.91e-16	–	19.0	–	0.46	–	34.85
XMM-106[c]	60	95	1:33:48.35	30:39:28.44	59600 ± 797	5.32e-01 ± 7.20e-03	<4.97e-13	<4.80e-13	14.0	14.0	0.74	0.63	36.00	35.95
XMM-107	61	96	1:33:48.49	30:33:04.39	1419 ± 62	1.03e-02 ± 4.59e-04	1.56e-14	1.28e-14	60.0	40.0	0.74	0.98	37.20	36.52
XMM-108[t]	62	97	1:33:49.75	30:30:49.66	54 ± 39	4.15e-04 ± 2.93e-04	4.94e-16	<3.59e-16	73.0	56.0	–	0.59	36.28	36.24
XMM-109	63	98	1:33:49.90	30:30:16.72	52 ± 17	4.43e-04 ± 1.44e-04	8.48e-16	<3.71e-16	54.0	46.0	–	0.95	35.74	35.69
XMM-110[t]	64	99	1:33:50.12	30:35:28.58	163 ± 55	1.34e-03 ± 4.61e-04	9.01e-16	5.77e-15	48.0	50.0	0.83	0.74	36.30	36.36
XMM-111	65	100	1:33:51.06	30:43:56.17	92 ± 21	7.26e-04 ± 1.71e-04	1.20e-15	6.56e-16	50.0	48.0	0.63	0.55	36.73	36.70
XMM-112	66	101	1:33:51.67	30:30:59.65	90 ± 22	6.65e-04 ± 1.62e-04	1.12e-15	7.42e-16	59.0	58.0	1.65	1.00	36.11	36.07
XMM-113	67	102	1:33:51.71	30:30:43.45	23 ± 16	2.00e-04 ± 1.35e-04	<4.78e-16	<2.52e-16	45.0	44.0	–	0.74	35.98	35.97
XMM-114	68	–	1:33:52.53	30:56:35.22	87 ± 19	8.80e-04 ± 1.95e-04	1.40e-15	9.14e-16	109.0	–	–	–	36.43	–
XMM-115	–	103	1:33:52.56	30:28:38.44	19 ± 14	1.31e-04 ± 1.02e-04	<2.89e-16	<1.96e-16	–	40.0	–	0.44	–	35.62
XMM-116	69	104	1:33:54.47	30:33:49.12	667 ± 53	4.99e-03 ± 4.11e-04	7.92e-15	5.99e-15	47.0	49.0	0.82	0.83	36.51	36.58
XMM-117	–	106	1:33:54.69	30:18:50.96	69 ± 16	8.27e-04 ± 2.04e-04	1.25e-15	8.58e-16	–	72.0	–	0.91	–	36.07
XMM-118	70	105	1:33:54.84	30:45:19.02	633 ± 43	3.91e-03 ± 2.72e-04	6.36e-15	3.66e-15	21.0	38.0	0.83	0.76	36.57	36.93
XMM-119	71	107	1:33:54.93	30:33:10.20	4344 ± 82	4.06e-02 ± 7.81e-04	6.82e-14	4.43e-14	20.0	26.0	0.83	0.87	36.91	36.91
XMM-120[c]	72	108	1:33:55.01	30:39:57.33	27602 ± 814	2.30e-01 ± 6.45e-03	<3.52e-13	<2.82e-13	32.0	32.0	–	0.79	35.65	35.74
XMM-121	–	109	1:33:55.29	30:16:48.95	26 ± 14	3.54e-04 ± 1.86e-04	<9.02e-16	<2.38e-16	–	31.0	–	0.54	–	35.28
XMM-122	73	110	1:33:56.44	30:21:24.72	177 ± 26	1.67e-03 ± 2.51e-04	2.17e-15	1.14e-15	57.0	58.0	–	0.93	36.34	36.32
XMM-123[t]	74	111	1:33:56.97	30:34:58.69	21 ± 40	1.29e-04 ± 2.62e-04	1.40e-16	<2.90e-16	31.0	31.0	0.67	1.02	36.08	36.25
XMM-124	75	112	1:33:57.13	30:40:48.54	23 ± 15	1.50e-04 ± 1.19e-04	<4.04e-16	8.68e-17	44.0	42.0	1.16	0.83	36.00	35.98
XMM-125	76	113	1:33:57.13	30:35:06.05	12 ± 22	7.32e-05 ± 1.44e-04	<4.23e-16	<2.30e-16	21.0	19.0	–	0.50	36.11	36.03
XMM-126	–	114	1:33:57.41	31:00:55.81	12 ± 11	1.55e-04 ± 1.59e-04	<5.64e-16	<3.00e-16	–	60.0	–	0.51	–	36.04
XMM-127	77	115	1:33:58.06	30:32:09.64	68 ± 21	5.08e-04 ± 1.68e-04	7.32e-16	6.73e-16	24.0	24.0	0.40	0.37	36.28	36.28
XMM-128	78	116	1:33:58.07	30:37:54.57	216 ± 32	1.88e-03 ± 2.77e-04	3.72e-15	9.02e-16	16.0	22.0	1.19	0.95	36.04	36.12
XMM-129	80	117	1:33:58.14	30:36:23.30	183 ± 31	1.18e-03 ± 2.05e-04	1.65e-15	1.13e-15	8.0	15.0	0.96	0.98	35.46	35.59
XMM-130	79	–	1:33:58.15	30:48:36.45	75 ± 21	6.83e-04 ± 1.96e-04	8.63e-16	8.87e-16	58.0	–	–	–	36.63	–
XMM-131	82	118	1:33:58.18	30:51:53.73	140 ± 23	1.32e-03 ± 2.19e-04	2.19e-15	1.31e-15	56.0	54.0	1.07	0.91	36.18	36.16
XMM-132	81	119	1:33:58.52	30:33:32.60	1152 ± 51	1.03e-02 ± 4.68e-04	1.80e-14	1.13e-14	34.0	48.0	0.73	0.52	36.23	36.48
XMM-133	–	120	1:33:59.15	30:32:42.06	52 ± 22	4.58e-04 ± 1.99e-04	8.37e-16	<3.78e-16	–	39.0	–	0.50	–	36.23
XMM-134	83	121	1:33:59.93	30:34:21.18	32 ± 26	1.98e-04 ± 1.78e-04	<6.25e-16	<4.27e-16	31.0	–	0.63	–	36.72	–
XMM-135	85	124	1:34:00.00	30:47:23.28	245 ± 31	1.72e-03 ± 2.26e-04	2.85e-15	1.79e-15	43.0	46.0	–	1.00	36.08	36.15
XMM-136	84	123	1:34:00.19	30:42:18.52	653 ± 40	4.43e-03 ± 2.77e-04	7.70e-15	4.72e-15	32.0	36.0	1.23	0.93	36.28	36.27

ID	L10	LL14	RA	Dec	0.2-2.0 Cts	0.2-2.0 Ct Rate (s^{-1})	0.2-2.0 Flux ergs s cm^{-2}	0.35-2.0 Flux ergs s cm^{-2}	D(pc) L10	D(pc) LL14	[SII]/Hα L10	[SII]/Hα LL14	log(L(Hα) (ergs s^{-1})) L10	log(L(Hα) (ergs s^{-1})) LL14
XMM-137[t]	–	122	1:34:00.25	30:39:28.87	451 ± 96	2.93e-03 ± 7.65e-04	3.69e-15	3.33e-14	–	40.0	–	0.81	–	36.09
XMM-138	–	125	1:34:00.58	30:50:42.87	77 ± 18	6.10e-04 ± 1.49e-04	5.29e-16	4.08e-16	–	23.0	–	0.93	–	35.04
XMM-139	86	126	1:34:00.60	30:49:04.29	259 ± 29	1.82e-03 ± 2.02e-04	3.28e-15	1.52e-15	13.0	12.0	0.80	0.60	34.98	34.88
XMM-140[t]	87	127	1:34:01.26	30:35:14.97	2298 ± 411	1.64e-02 ± 2.99e-03	2.05e-14	7.15e-15	48.0	48.0	0.90	0.85	36.04	36.19
XMM-141	–	128	1:34:02.10	30:28:34.52	25 ± 13	1.67e-04 ± 9.73e-05	<4.46e-16	<7.58e-17	–	37.0	–	0.48	–	35.44
XMM-142	88	129	1:34:02.58	30:31:02.62	81 ± 19	1.05e-03 ± 2.56e-04	1.66e-15	7.42e-16	60.0	53.0	0.96	0.89	36.23	36.24
XMM-143	89	130	1:34:03.23	30:36:26.53	1330 ± 97	8.78e-03 ± 6.48e-04	1.62e-14	8.79e-15	92.0	90.0	–	0.49	37.11	37.11
XMM-144	90	131	1:34:03.52	30:44:42.40	235 ± 31	1.38e-03 ± 1.84e-04	2.67e-15	1.27e-15	42.0	44.0	1.03	0.79	36.04	36.08
XMM-145	91	132	1:34:04.15	30:32:57.50	298 ± 30	2.08e-03 ± 2.13e-04	4.27e-15	2.14e-15	36.0	32.0	–	1.00	35.36	35.44
XMM-146	–	133	1:34:04.88	30:58:30.71	13 ± 12	1.24e-04 ± 1.25e-04	<5.69e-16	<9.22e-17	–	72.0	–	0.46	–	36.07
XMM-147	–	134	1:34:05.55	31:07:25.08	136 ± 16	3.84e-03 ± 4.75e-04	1.63e-14	6.97e-15	–	55.0	–	0.71	–	35.60
XMM-148	92	135	1:34:07.30	30:36:20.14	220 ± 33	1.62e-03 ± 2.44e-04	2.43e-15	1.49e-15	101.0	96.0	0.71	0.78	36.89	36.92
XMM-149	93	136	1:34:07.47	30:37:07.61	407 ± 36	2.26e-03 ± 1.99e-04	3.78e-15	2.48e-15	20.0	16.0	0.95	0.87	35.32	35.26
XMM-150[n]	–	137	1:34:07.98	31:01:03.72	42 ± 13	5.43e-04 ± 2.07e-04	<1.42e-15	9.61e-16	–	54.0	–	0.55	–	36.06
XMM-151	94	138	1:34:08.36	30:46:32.70	1267 ± 51	6.98e-03 ± 2.82e-04	1.26e-14	7.60e-15	20.0	19.0	0.75	0.50	35.71	35.63
XMM-152[t]	95	139	1:34:10.14	30:47:16.78	247 ± 56	1.46e-03 ± 3.41e-04	1.71e-15	1.64e-15	23.0	26.0	0.83	0.78	35.60	35.74
XMM-153	96	140	1:34:10.65	30:42:23.51	2947 ± 69	2.05e-02 ± 4.91e-04	3.75e-14	2.13e-14	18.0	23.0	1.25	1.17	36.70	36.70
XMM-154	97	141	1:34:10.92	30:39:00.70	139 ± 25	9.47e-04 ± 1.76e-04	1.53e-15	9.73e-16	14.0	16.0	1.15	0.74	35.40	35.56
XMM-155	–	142	1:34:11.21	30:24:15.32	46 ± 17	4.14e-04 ± 1.62e-04	9.80e-16	5.95e-16	–	42.0	–	0.62	–	35.45
XMM-156	–	143	1:34:12.28	31:02:43.42	14 ± 10	2.20e-04 ± 1.67e-04	<3.57e-16	<2.71e-16	–	55.0	–	0.48	–	35.81
XMM-157	98	–	1:34:12.69	30:35:11.98	44 ± 20	2.63e-04 ± 1.20e-04	6.50e-16	<2.69e-16	67.0	–	0.46	–	36.58	–
XMM-158	–	144	1:34:12.90	30:23:24.28	32 ± 14	2.83e-04 ± 1.32e-04	8.24e-16	<2.42e-16	–	46.0	–	0.50	–	35.63
XMM-159	99	145	1:34:13.02	30:48:36.11	99 ± 26	6.18e-04 ± 1.63e-04	9.80e-16	6.50e-16	51.0	46.0	–	0.69	36.49	36.48
XMM-160	100	146	1:34:13.65	30:43:27.01	98 ± 21	6.08e-04 ± 1.35e-04	9.70e-16	5.25e-16	26.0	27.0	0.87	0.79	35.62	35.63
XMM-161	101	147	1:34:13.71	30:48:17.47	106 ± 24	6.64e-04 ± 1.54e-04	8.99e-16	4.48e-16	58.0	62.0	–	0.76	36.51	36.70
XMM-162	–	148	1:34:13.85	30:30:39.82	17 ± 13	1.02e-04 ± 8.74e-05	<2.10e-16	<1.22e-16	–	16.0	–	0.39	–	35.22
XMM-163	102	149	1:34:14.10	30:34:30.92	70 ± 23	4.41e-04 ± 1.43e-04	5.47e-16	4.87e-16	39.0	40.0	0.46	0.52	36.71	36.74
XMM-164	103	150	1:34:14.35	30:41:53.59	53 ± 21	3.44e-04 ± 1.36e-04	1.11e-15	<3.93e-16	48.0	44.0	1.08	0.85	36.00	35.91
XMM-165	105	152	1:34:14.37	30:53:52.65	301 ± 28	2.73e-03 ± 2.63e-04	4.35e-15	2.85e-15	50.0	58.0	1.02	1.00	36.45	36.50
XMM-166	104	151	1:34:14.38	30:39:41.56	132 ± 24	9.10e-04 ± 1.75e-04	1.63e-15	7.52e-16	39.0	38.0	1.05	1.05	36.00	35.99
XMM-167	–	153	1:34:14.55	30:44:36.18	24 ± 16	1.44e-04 ± 1.04e-04	<3.24e-16	<1.29e-16	–	51.0	–	0.74	–	36.10
XMM-168	106	154	1:34:14.67	30:31:50.92	76 ± 20	5.81e-04 ± 1.56e-04	8.91e-16	6.66e-16	66.0	66.0	–	1.10	35.93	35.85
XMM-169	107	155	1:34:15.69	30:33:00.67	279 ± 31	1.60e-03 ± 1.83e-04	2.64e-15	1.97e-15	33.0	34.0	0.74	0.69	35.97	36.01
XMM-170	108	156	1:34:16.31	30:52:32.74	109 ± 23	7.47e-04 ± 1.61e-04	1.27e-15	6.49e-16	77.0	80.0	0.80	0.60	36.56	36.84
XMM-171	110	158	1:34:16.46	30:33:55.07	182 ± 30	1.16e-03 ± 1.96e-04	1.75e-15	1.26e-15	54.0	52.0	–	0.52	36.71	36.78
XMM-172[x]	109	157	1:34:16.50	30:51:53.86	937 ± 48	6.29e-03 ± 3.23e-04	<1.08e-14	<7.74e-15	25.0	32.0	0.28	0.40	36.72	36.86
XMM-173	111	159	1:34:17.50	30:41:22.64	436 ± 34	2.76e-03 ± 2.21e-04	5.02e-15	2.83e-15	51.0	52.0	1.04	0.89	36.38	36.38
XMM-174	112	160	1:34:18.32	30:54:05.78	27 ± 14	3.10e-04 ± 1.61e-04	<7.11e-16	<3.18e-16	84.0	80.0	–	0.98	36.15	36.08
XMM-175	113	161	1:34:19.28	30:33:45.91	19 ± 21	1.27e-04 ± 1.32e-04	<3.20e-16	<1.83e-16	38.0	40.0	0.62	0.46	36.81	36.89
XMM-176	–	162	1:34:19.45	30:52:48.89	91 ± 22	6.71e-04 ± 1.64e-04	8.95e-16	6.93e-16	–	75.0	–	0.87	–	36.09
XMM-177	–	163	1:34:19.68	30:33:41.51	53 ± 23	3.35e-04 ± 1.46e-04	6.82e-16	<4.30e-16	–	38.0	–	0.36	–	36.82
XMM-178	114	164	1:34:19.87	30:33:56.02	23 ± 21	1.36e-04 ± 1.40e-04	<4.85e-16	<1.94e-16	22.0	30.0	0.74	0.69	36.49	36.63
XMM-179	116	166	1:34:22.94	30:54:22.95	172 ± 25	2.49e-03 ± 3.81e-04	3.60e-15	2.92e-15	42.0	10.0	0.86	0.89	34.99	34.73
XMM-180	115	165	1:34:23.34	30:25:26.85	152 ± 22	1.36e-03 ± 2.01e-04	1.91e-15	1.57e-15	47.0	50.0	–	0.78	35.92	35.96
XMM-181	–	167	1:34:24.08	30:33:24.41	63 ± 23	3.88e-04 ± 1.44e-04	9.58e-16	<4.45e-16	–	60.0	–	0.44	–	36.32
XMM-182	–	168	1:34:24.48	30:48:58.35	23 ± 13	1.76e-04 ± 1.08e-04	<3.27e-16	<1.24e-16	–	80.0	–	0.48	–	36.56
XMM-183	117	169	1:34:25.40	30:54:57.44	110 ± 23	1.20e-03 ± 2.56e-04	1.44e-15	1.10e-15	66.0	64.0	0.78	0.87	36.78	36.63

ID	L10	LL14	RA	Dec	0.2-2.0 Cts	0.2-2.0 Ct Rate (s^{-1})	0.2-2.0 Flux ergs s cm^{-2}	0.35-2.0 Flux ergs s cm^{-2}	D(pc) L10	D(pc) LL14	[SII]/Hα L10	[SII]/Hα LL14	log(L(Hα) (ergs s^{-1})) L10	log(L(Hα) (ergs s^{-1})) LL14
XMM-184[n]	118	170	1:34:25.41	30:48:30.95	46 ± 19	3.69e-04 ± 1.47e-04	7.96e-16	<4.65e-16	53.0	44.0	1.06	0.93	35.95	35.88
XMM-185	119	171	1:34:25.82	30:33:17.02	342 ± 31	2.43e-03 ± 2.28e-04	2.87e-15	2.79e-15	33.0	26.0	–	0.49	35.38	35.15
XMM-186	120	172	1:34:29.61	30:41:33.38	27 ± 16	1.86e-04 ± 1.14e-04	<3.63e-16	<2.21e-16	43.0	42.0	0.82	0.59	36.08	36.22
XMM-187[t]	–	173	1:34:30.22	30:35:10.51	163 ± 46	9.79e-04 ± 2.92e-04	1.14e-15	4.40e-16	–	85.0	–	0.54	–	36.05
XMM-188	121	175	1:34:30.29	30:35:44.80	119 ± 26	7.07e-04 ± 1.54e-04	1.26e-15	4.97e-16	54.0	52.0	1.04	1.00	36.18	36.19
XMM-189	122	174	1:34:30.93	30:56:39.82	164 ± 22	1.82e-03 ± 2.44e-04	3.16e-15	1.78e-15	111.0	34.0	–	0.98	36.84	35.83
XMM-190	123	176	1:34:32.63	30:35:30.37	154 ± 25	8.41e-04 ± 1.42e-04	1.21e-15	9.19e-16	41.0	40.0	–	1.02	36.00	35.92
XMM-191	124	177	1:34:33.03	30:46:37.65	94 ± 32	7.88e-04 ± 3.30e-04	1.36e-15	9.95e-16	11.0	16.0	0.66	0.62	36.65	36.73
XMM-192	125	178	1:34:35.52	30:52:10.97	130 ± 23	1.33e-03 ± 2.51e-04	2.83e-15	1.25e-15	39.0	38.0	–	0.87	35.71	35.69
XMM-193	126	179	1:34:36.22	30:36:23.56	38 ± 20	2.19e-04 ± 1.19e-04	<4.85e-16	<1.91e-16	46.0	40.0	–	0.60	36.04	35.86
XMM-194	–	180	1:34:37.40	30:44:11.03	21 ± 13	1.82e-04 ± 1.13e-04	<4.29e-16	<2.39e-16	–	61.0	–	0.48	–	36.52
XMM-195	127	181	1:34:38.73	30:37:56.82	90 ± 23	5.27e-04 ± 1.38e-04	6.83e-16	4.86e-16	86.0	80.0	–	0.41	36.63	36.57
XMM-196	–	182	1:34:39.69	30:39:17.55	37 ± 15	2.42e-04 ± 1.10e-04	6.81e-16	<2.08e-16	–	64.0	–	0.71	–	35.95
XMM-197	–	183	1:34:39.94	31:06:02.72	12 ± 8	2.08e-04 ± 1.35e-04	<4.85e-16	<1.56e-16	–	53.0	–	0.93	–	35.76
XMM-198	128	184	1:34:40.74	30:43:36.44	62 ± 20	5.32e-04 ± 1.75e-04	7.17e-16	<3.25e-16	22.0	36.0	0.77	0.87	36.41	36.73
XMM-199	129	185	1:34:41.09	30:43:26.33	669 ± 36	5.45e-03 ± 2.96e-04	9.93e-15	6.70e-15	39.0	50.0	1.07	0.91	36.86	36.96
XMM-200	130	186	1:34:41.23	30:43:55.38	31 ± 16	2.99e-04 ± 1.55e-04	<4.38e-16	<2.36e-16	35.0	32.0	–	0.72	35.57	35.80
XMM-201	131	–	1:34:41.89	30:37:35.25	41 ± 17	2.16e-04 ± 1.13e-04	4.28e-16	<2.56e-16	156.0	–	–	–	36.92	–
XMM-202	–	187	1:34:42.68	30:40:51.50	21 ± 14	1.64e-04 ± 1.15e-04	<4.10e-16	<2.25e-16	–	39.0	–	0.62	–	35.58
XMM-203[t]	–	188	1:34:44.02	31:01:48.89	1 ± 12	2.39e-05 ± 1.76e-04	1.08e-17	<7.50e-17	–	80.0	–	0.66	–	35.86
XMM-204	132	–	1:34:44.62	30:42:38.79	11 ± 11	8.86e-05 ± 8.62e-05	<3.31e-16	<5.88e-17	55.0	–	–	–	36.46	–
XMM-205[x]	–	189	1:34:45.40	30:35:35.18	93 ± 24	6.12e-04 ± 1.62e-04	<1.26e-15	<6.01e-16	–	49.0	–	0.91	–	35.65
XMM-206	–	190	1:34:45.88	30:57:19.13	32 ± 13	3.52e-04 ± 1.65e-04	8.26e-16	4.52e-16	–	50.0	–	0.91	–	35.66
XMM-207	–	191	1:34:47.24	30:34:24.98	32 ± 14	2.89e-04 ± 1.33e-04	6.83e-16	<3.05e-16	–	37.0	–	0.44	–	35.59
XMM-208	–	192	1:34:50.48	31:07:38.63	13 ± 7	2.49e-04 ± 1.42e-04	<2.61e-16	<8.24e-17	–	55.0	–	0.45	–	35.76
XMM-209[t]	–	193	1:34:52.48	30:50:22.22	59 ± 33	7.29e-04 ± 4.31e-04	6.54e-16	<1.90e-16	–	84.0	–	0.98	–	35.89
XMM-210	133	–	1:34:54.88	30:41:16.95	47 ± 17	3.81e-04 ± 1.41e-04	8.78e-16	6.41e-16	75.0	–	–	–	36.84	–
XMM-211[n]	134	194	1:34:56.44	30:36:23.16	66 ± 18	7.32e-04 ± 1.97e-04	<1.36e-15	8.27e-16	58.0	56.0	–	0.91	35.83	35.81
XMM-212[n]	–	195	1:34:58.60	31:10:09.50	38 ± 12	1.13e-03 ± 3.50e-04	<1.57e-15	1.11e-15	–	44.0	–	0.60	–	35.66
XMM-213	–	196	1:34:59.19	30:40:16.49	43 ± 16	3.84e-04 ± 1.58e-04	8.01e-16	6.61e-16	–	36.0	–	0.79	–	35.60
XMM-214	135	197	1:35:00.36	30:40:04.97	47 ± 16	4.70e-04 ± 1.57e-04	9.16e-16	5.52e-16	65.0	58.0	–	0.68	36.32	36.27
XMM-215	–	198	1:35:00.40	31:02:36.37	7 ± 9	1.17e-04 ± 1.53e-04	<3.97e-16	<1.74e-16	–	72.0	–	0.52	–	35.94
XMM-216	136	–	1:35:01.22	30:38:17.07	23 ± 11	2.25e-04 ± 1.13e-04	4.79e-16	<2.76e-16	128.0	–	–	–	36.72	–
XMM-217[t]	–	199	1:35:01.82	30:39:53.94	24 ± 24	2.20e-04 ± 2.22e-04	1.26e-16	<1.48e-16	–	80.0	–	0.56	–	36.46
XMM-218[x]	137	–	1:35:02.80	30:37:08.60	181 ± 21	2.67e-03 ± 3.24e-04	<3.45e-15	<3.31e-15	127.0	–	–	–	36.67	–

[c] Flux is contaminated by nearby bright X-ray source, but source has a previous X-ray detection. Flux is an upper limit.

[b] Unrealistic source count errors from `emldetect` in at least one individual band. Source count errors pegged to total count values.

[n] Determined to be a nondetection via by-eye catalog checking. Flux is an upper limit.

[t] Total counts in the full band are discrepant by a factor of two from the summation of counts in each individual band due an `emldetect` merging issue. Total counts in the 0.2-2.0 keV band are reported as the sum of counts in the 0.2-0.5 keV, 0.5-1.0 keV, and 1.0-2.0 keV band.

[x] Flux is contaminated by nearby bright X-ray source, but source does not have a previous X-ray detection. Flux is an upper limit.

Table 3: All 105 3σ SNRs detected in our sample. Columns 1-3: ID number from this catalog, and the RA and Dec from this catalog. Column 4: source counts and associated errors in the 0.2-2.0 keV band (used for detection). Column 5: source counts and associated errors in the 0.35-2.0 keV band (used for comparison to L10). Columns 6-8: source counts and errors in the 0.3-0.7 keV, 0.7-1.1 keV, and 1.1-4.2 keV bands, which are used for computing the HRs shown in Figure **??**. Columns 9-10: HRs and errors in the aforementioned bands (HR1 = (M-S)/(H+M+S), HR2 = (H-M)/(H+M+S)). Columns 11-12: HRs and errors computed from the 0.2-0.5 keV, 0.5-1.0 keV, and 1.0-2.0 keV bands ($HR1_{XMM}$ = (M-S)/(S+M), $HR2_{XMM}$ = (H-M)/(H+M)). Column 13: measurement level in L10: 3σ, 2σ, or upper limit (<).

ID	RA	Dec	0.2-2.0 keV Cts	0.35-2.0 keV Cts	0.3-0.7 keV Cts	0.7-1.1 keV Cts	1.1-4.2 keV Cts	HR1	HR2	$HR1_{XMM}$	$HR2_{XMM}$	L10 Detect
XMM-003	1:32:30.83	30:27:45.99	107 ± 19	98 ± 19	55 ± 13	48 ± 11	15 ± 11	-0.14 ± 0.02	-0.29 ± 0.01	0.49 ± 0.05	0.18 ± 0.04	–
XMM-004	1:32:31.41	30:35:32.90	66 ± 19	53 ± 18	10 ± 10	25 ± 9	13 ± 16	0.04 ± 0.02	-0.34 ± 0.02	–	–	<
XMM-006	1:32:37.36	30:18:03.10	296 ± 23	286 ± 22	45 ± 9	104 ± 12	222 ± 20	-0.16 ± 0.02	-0.31 ± 0.02	0.47 ± 0.01	-0.47 ± 0.01	–
XMM-009	1:32:40.53	30:16:37.20	74 ± 13	79 ± 13	12 ± 6	14 ± 6	91 ± 14	0.10 ± 0.03	-0.21 ± 0.03	0.90 ± 0.07	0.60 ± 0.03	–
XMM-015	1:32:46.61	30:34:37.00	253 ± 26	207 ± 25	163 ± 19	35 ± 10	27 ± 14	-0.31 ± 0.05	-0.16 ± 0.05	0.47 ± 0.22	0.79 ± 0.04	3σ
XMM-019	1:32:53.36	30:48:23.06	53 ± 15	41 ± 14	18 ± 9	22 ± 8	8 ± 9	0.02 ± 0.06	-0.33 ± 0.09	–	–	2σ
XMM-022	1:32:55.96	30:40:33.57	134 ± 23	123 ± 23	59 ± 14	32 ± 10	61 ± 18	-0.30 ± 0.07	-0.05 ± 0.10	0.60 ± 0.06	0.27 ± 0.04	<
XMM-023	1:32:56.12	30:33:30.44	68 ± 20	57 ± 18	32 ± 12	19 ± 10	23 ± 14	-0.73 ± 0.05	-0.01 ± 0.05	–	–	–
XMM-024	1:32:57.10	30:39:25.87	474 ± 32	443 ± 31	241 ± 21	203 ± 19	42 ± 15	0.18 ± 0.08	0.39 ± 0.09	0.57 ± 0.03	0.22 ± 0.02	3σ
XMM-027	1:33:00.40	30:44:07.57	407 ± 33	363 ± 32	245 ± 24	113 ± 17	100 ± 24	0.08 ± 0.01	0.75 ± 0.02	0.71 ± 0.04	0.41 ± 0.02	3σ
XMM-030	1:33:02.93	30:32:29.65	93 ± 20	83 ± 21	19 ± 11	66 ± 13	10 ± 12	0.04 ± 0.12	-0.40 ± 0.13	–	–	3σ
XMM-031	1:33:03.58	30:31:18.27	225 ± 27	192 ± 27	113 ± 19	58 ± 14	57 ± 17	-0.05 ± 0.08	-0.05 ± 0.12	0.43 ± 0.04	0.07 ± 0.04	<
XMM-032	1:33:04.07	30:39:51.65	217 ± 27	230 ± 28	53 ± 15	105 ± 16	66 ± 21	-0.07 ± 0.06	-0.25 ± 0.08	0.73 ± 0.11	0.55 ± 0.04	3σ
XMM-033	1:33:07.55	30:42:52.51	71 ± 23	50 ± 20	23 ± 11	7 ± 9	34 ± 19	-0.33 ± 0.10	-0.09 ± 0.12	–	–	<
XMM-034	1:33:08.77	30:12:15.64	928 ± 36	862 ± 35	584 ± 28	281 ± 19	41 ± 11	-0.61 ± 0.14	-0.05 ± 0.12	0.63 ± 0.01	-0.64 ± 0.01	–
XMM-035	1:33:08.93	30:26:57.31	181 ± 26	156 ± 25	59 ± 15	79 ± 14	55 ± 19	-0.05 ± 0.12	-0.34 ± 0.14	0.33 ± 0.53	0.94 ± 0.04	2σ
XMM-038[e]	1:33:10.16	30:42:22.26	372 ± 35	333 ± 33	145 ± 145	126 ± 126	114 ± 25	-0.13 ± 0.15	-0.14 ± 0.19	0.35 ± 0.02	-0.75 ± 0.03	3σ
XMM-039	1:33:11.16	30:39:43.41	1807 ± 56	1614 ± 54	1096 ± 42	515 ± 30	91 ± 21	0.03 ± 0.10	0.68 ± 0.14	0.43 ± 0.01	0.10 ± 0.01	3σ
XMM-041	1:33:11.80	30:38:40.48	21032 ± 190	20152 ± 190	8698 ± 133	9787 ± 137	2230 ± 60	-0.17 ± 0.12	-0.22 ± 0.14	0.54 ± 0.00	0.29 ± 0.00	3σ
XMM-042	1:33:13.46	30:28:13.12	99 ± 22	76 ± 21	33 ± 14	29 ± 11	45 ± 18	-0.26 ± 0.15	-0.20 ± 0.16	–	–	–
XMM-046	1:33:17.44	30:31:28.50	79 ± 22	61 ± 20	22 ± 13	13 ± 10	75 ± 19	0.30 ± 0.14	0.03 ± 0.17	–	–	<
XMM-050	1:33:18.94	30:46:51.88	92 ± 19	65 ± 19	46 ± 13	17 ± 8	61 ± 15	-0.08 ± 0.11	-0.11 ± 0.15	–	–	2σ
XMM-054[t]	1:33:21.33	30:30:31.63	1036 ± 341	68 ± 21	49 ± 16	910 ± 303	76 ± 22	-0.07 ± 0.19	-0.29 ± 0.19	–	–	–
XMM-057	1:33:22.67	30:27:04.00	87 ± 24	53 ± 20	42 ± 14	25 ± 13	27 ± 17	-0.34 ± 0.14	-0.11 ± 0.15	–	–	<
XMM-059	1:33:24.01	30:36:56.81	72 ± 21	47 ± 18	15 ± 11	18 ± 9	40 ± 20	-0.01 ± 0.19	-0.27 ± 0.19	–	–	–
XMM-065	1:33:28.11	30:31:33.53	749 ± 42	729 ± 42	430 ± 30	255 ± 23	81 ± 22	-0.06 ± 0.28	-0.06 ± 0.31	0.36 ± 0.02	-0.03 ± 0.02	3σ
XMM-066	1:33:28.92	30:47:43.95	736 ± 36	660 ± 35	464 ± 27	200 ± 19	57 ± 17	-0.11 ± 0.24	-0.02 ± 0.29	0.62 ± 0.02	0.24 ± 0.01	3σ
XMM-067	1:33:29.08	30:42:15.99	3706 ± 78	3568 ± 76	1546 ± 50	1692 ± 50	452 ± 34	-0.57 ± 0.22	0.16 ± 0.20	0.80 ± 0.01	0.44 ± 0.00	3σ
XMM-068	1:33:29.48	30:49:10.63	2170 ± 59	1987 ± 56	1127 ± 41	790 ± 34	149 ± 22	0.09 ± 0.20	0.23 ± 0.26	0.64 ± 0.01	0.31 ± 0.01	3σ
XMM-069	1:33:29.79	31:01:53.00	52 ± 14	43 ± 14	27 ± 9	8 ± 6	14 ± 10	0.25 ± 0.14	0.28 ± 0.22	–	–	–
XMM-073	1:33:31.30	30:33:32.42	7361 ± 106	7084 ± 118	3349 ± 71	2741 ± 63	1276 ± 51	-0.07 ± 0.46	0.06 ± 0.49	0.49 ± 0.00	0.19 ± 0.00	3σ
XMM-074	1:33:31.34	30:42:18.33	95 ± 27	103 ± 28	32 ± 16	43 ± 16	37 ± 17	-0.03 ± 0.39	0.20 ± 0.46	–	–	2σ
XMM-075	1:33:32.17	30:31:02.62	172 ± 30	172 ± 31	69 ± 17	77 ± 17	73 ± 23	-0.10 ± 0.38	0.32 ± 0.43	0.56 ± 0.06	0.17 ± 0.04	<
XMM-076	1:33:34.99	30:29:54.55	134 ± 26	119 ± 24	84 ± 18	29 ± 12	35 ± 18	-0.06 ± 0.27	0.37 ± 0.33	–	–	–
XMM-078	1:33:35.14	30:23:07.44	96 ± 20	94 ± 20	22 ± 12	38 ± 10	57 ± 18	0.27 ± 0.41	-0.19 ± 0.47	–	–	<
XMM-079[t]	1:33:35.59	30:42:29.14	276 ± 56	571 ± 55	128 ± 20	113 ± 18	35 ± 17	-0.06 ± 0.38	0.31 ± 0.45	0.84 ± 0.07	0.50 ± 0.03	3σ
XMM-080	1:33:35.61	30:49:22.96	65 ± 18	57 ± 18	19 ± 9	23 ± 9	33 ± 14	-0.04 ± 0.26	0.54 ± 0.35	–	–	2σ
XMM-081[t]	1:33:35.81	30:31:13.67	322 ± 68	632 ± 74	116 ± 23	56 ± 17	149 ± 27	0.01 ± 0.39	0.09 ± 0.48	0.85 ± 0.10	0.55 ± 0.03	–
XMM-082	1:33:35.97	30:36:26.68	1746 ± 56	1718 ± 55	594 ± 33	782 ± 35	413 ± 35	0.15 ± 0.41	-0.05 ± 0.52	0.46 ± 0.01	0.09 ± 0.01	3σ
XMM-083[t]	1:33:36.92	30:32:54.24	3016 ± 531	788 ± 64	84 ± 22	338 ± 33	2592 ± 475	-0.06 ± 0.46	-0.01 ± 0.44	0.64 ± 0.03	0.30 ± 0.02	3σ
XMM-084	1:33:37.02	30:33:10.04	100 ± 27	66 ± 23	28 ± 17	23 ± 13	18 ± 18	-0.32 ± 0.34	0.30 ± 0.35	–	–	–
XMM-085	1:33:37.68	30:40:09.50	234 ± 30	251 ± 30	39 ± 15	106 ± 17	119 ± 23	-0.50 ± 0.28	0.07 ± 0.25	0.73 ± 0.06	0.37 ± 0.04	3σ
XMM-088	1:33:39.59	30:34:26.02	126 ± 28	87 ± 27	72 ± 19	38 ± 13	16 ± 18	-0.07 ± 0.45	0.10 ± 0.48	–	–	–
XMM-089	1:33:39.80	30:31:19.05	243 ± 30	209 ± 30	107 ± 19	54 ± 14	40 ± 18	0.33 ± 0.35	-0.41 ± 0.33	0.61 ± 0.04	0.24 ± 0.03	–

ID	RA	Dec	0.2-2.0 keV Cts	0.35-2.0 keV Cts	0.3-0.7 keV Cts	0.7-1.1 keV Cts	1.1-4.2 keV Cts	HR1	HR2	$HR1_{XMM}$	$HR2_{XMM}$	L10 Detect
XMM-090	1:33:40.54	30:10:48.35	138 ± 17	117 ± 16	66 ± 11	44 ± 8	10 ± 9	-0.12 ± 0.36	0.30 ± 0.42	0.55 ± 0.02	-0.63 ± 0.03	–
XMM-095	1:33:41.44	30:42:20.77	696 ± 59	692 ± 61	253 ± 34	215 ± 28	81 ± 20	0.14 ± 0.36	-0.18 ± 0.39	0.56 ± 0.03	0.04 ± 0.03	–
XMM-098	1:33:42.91	30:41:49.51	110 ± 25	99 ± 25	44 ± 14	47 ± 14	30 ± 17	-0.03 ± 0.34	0.44 ± 0.42	–	–	<
XMM-100[t]	1:33:43.70	30:36:11.50	955 ± 161	1425 ± 181	825 ± 123	84 ± 19	46 ± 19	-0.02 ± 0.46	0.04 ± 0.50	–	–	3σ
XMM-107	1:33:48.49	30:33:04.39	1419 ± 62	1434 ± 60	628 ± 40	635 ± 36	113 ± 26	0.00 ± 0.32	0.37 ± 0.47	0.51 ± 0.01	-0.37 ± 0.01	3σ
XMM-110[t]	1:33:50.12	30:35:28.58	163 ± 55	816 ± 127	38 ± 18	70 ± 16	54 ± 20	0.24 ± 0.23	-0.17 ± 0.30	–	–	2σ
XMM-111	1:33:51.06	30:43:56.17	92 ± 21	77 ± 21	45 ± 14	10 ± 10	34 ± 16	0.04 ± 0.35	0.29 ± 0.48	–	–	<
XMM-112	1:33:51.67	30:30:59.65	90 ± 22	61 ± 21	36 ± 14	31 ± 13	22 ± 13	0.10 ± 0.39	-0.14 ± 0.42	–	–	<
XMM-114	1:33:52.53	30:56:35.22	87 ± 19	78 ± 19	69 ± 14	8 ± 8	33 ± 15	0.17 ± 0.29	0.18 ± 0.46	0.20 ± 0.56	0.89 ± 0.08	<
XMM-116	1:33:54.47	30:33:49.12	667 ± 53	676 ± 52	420 ± 43	153 ± 20	35 ± 17	0.02 ± 0.36	0.20 ± 0.48	0.61 ± 0.02	-0.62 ± 0.02	3σ
XMM-117	1:33:54.69	30:18:50.96	69 ± 16	45 ± 15	12 ± 9	17 ± 8	16 ± 10	-0.02 ± 0.47	0.10 ± 0.54	–	–	–
XMM-118	1:33:54.84	30:45:19.02	633 ± 43	488 ± 37	258 ± 25	195 ± 21	70 ± 19	0.03 ± 0.41	0.06 ± 0.50	0.55 ± 0.02	0.19 ± 0.02	3σ
XMM-119	1:33:54.93	30:33:10.20	4344 ± 82	4015 ± 97	2202 ± 58	1611 ± 48	402 ± 32	-0.07 ± 0.35	0.35 ± 0.44	0.41 ± 0.00	0.21 ± 0.00	3σ
XMM-122	1:33:56.44	30:21:24.72	177 ± 26	136 ± 25	81 ± 17	64 ± 14	48 ± 18	0.15 ± 0.32	0.09 ± 0.42	0.46 ± 0.03	-0.76 ± 0.04	<
XMM-127	1:33:58.06	30:32:09.64	68 ± 21	57 ± 20	15 ± 12	16 ± 11	32 ± 19	-0.10 ± 0.36	0.30 ± 0.46	–	–	<
XMM-128	1:33:58.07	30:37:54.57	216 ± 32	143 ± 30	137 ± 23	62 ± 18	10 ± 12	-0.31 ± 0.35	-0.03 ± 0.28	–	–	3σ
XMM-129	1:33:58.14	30:36:23.30	183 ± 31	184 ± 30	58 ± 18	88 ± 18	99 ± 23	0.09 ± 0.35	-0.30 ± 0.27	0.52 ± 0.04	0.15 ± 0.03	3σ
XMM-130	1:33:58.15	30:48:36.45	75 ± 21	59 ± 20	10 ± 12	34 ± 12	31 ± 17	0.01 ± 0.42	0.13 ± 0.52	–	–	3σ
XMM-131	1:33:58.18	30:51:53.72	140 ± 23	125 ± 23	74 ± 15	41 ± 12	25 ± 18	0.26 ± 0.33	-0.30 ± 0.37	-0.18 ± 0.03	-0.47 ± 0.05	2σ
XMM-132	1:33:58.52	30:33:32.60	1152 ± 51	1106 ± 50	726 ± 39	251 ± 24	152 ± 26	0.03 ± 0.32	0.10 ± 0.41	0.60 ± 0.01	-0.53 ± 0.01	3σ
XMM-135	1:34:00.00	30:47:23.28	245 ± 31	210 ± 29	63 ± 16	65 ± 14	125 ± 25	0.00 ± 0.47	0.03 ± 0.52	0.27 ± 0.04	-0.43 ± 0.04	3σ
XMM-136	1:34:00.19	30:42:18.52	653 ± 40	575 ± 38	269 ± 26	282 ± 23	83 ± 20	-0.23 ± 0.39	0.24 ± 0.42	0.47 ± 0.02	-0.69 ± 0.02	3σ
XMM-137[t]	1:34:00.25	30:39:28.87	451 ± 96	3937 ± 512	18 ± 16	85 ± 18	347 ± 62	-0.05 ± 0.39	0.24 ± 0.48	–	–	–
XMM-138	1:34:00.58	30:50:42.87	77 ± 18	43 ± 17	8 ± 6	14 ± 7	54 ± 17	0.10 ± 0.32	0.19 ± 0.46	–	–	–
XMM-139	1:34:00.60	30:49:04.29	259 ± 29	183 ± 27	137 ± 20	33 ± 11	36 ± 17	-0.27 ± 0.21	0.34 ± 0.25	0.35 ± 0.03	0.08 ± 0.02	3σ
XMM-140[t]	1:34:01.26	30:35:14.97	2298 ± 411	840 ± 70	1864 ± 351	245 ± 31	188 ± 29	-0.05 ± 0.43	0.16 ± 0.49	0.58 ± 0.05	0.35 ± 0.03	3σ
XMM-142	1:34:02.58	30:31:02.62	81 ± 19	72 ± 19	44 ± 15	41 ± 12	19 ± 11	0.23 ± 0.26	-0.36 ± 0.26	0.76 ± 0.08	0.35 ± 0.04	3σ
XMM-143	1:34:03.23	30:36:26.53	1330 ± 97	1176 ± 104	682 ± 58	76 ± 17	72 ± 22	0.85 ± 0.06	-0.84 ± 0.08	0.15 ± 0.02	-0.11 ± 0.02	3σ
XMM-144	1:34:03.52	30:44:42.40	235 ± 31	181 ± 28	98 ± 19	35 ± 13	83 ± 22	-0.07 ± 0.40	0.22 ± 0.47	0.69 ± 0.03	-0.38 ± 0.04	3σ
XMM-145	1:34:04.15	30:32:57.50	298 ± 30	254 ± 28	176 ± 22	72 ± 14	54 ± 17	0.23 ± 0.35	-0.21 ± 0.41	0.35 ± 0.03	0.01 ± 0.03	3σ
XMM-147	1:34:05.55	31:07:25.08	136 ± 16	136 ± 16	59 ± 11	64 ± 10	15 ± 6	-0.08 ± 0.29	0.27 ± 0.38	0.48 ± 0.04	0.18 ± 0.03	–
XMM-148	1:34:07.30	30:36:20.14	220 ± 33	212 ± 33	128 ± 24	56 ± 17	41 ± 21	-0.06 ± 0.40	0.33 ± 0.43	0.56 ± 0.03	-0.34 ± 0.03	2σ
XMM-149	1:34:07.47	30:37:07.61	407 ± 36	371 ± 35	234 ± 25	102 ± 17	76 ± 22	0.07 ± 0.30	0.27 ± 0.42	0.49 ± 0.02	-0.70 ± 0.03	3σ
XMM-151	1:34:08.36	30:46:32.70	1267 ± 51	1130 ± 49	777 ± 38	384 ± 27	68 ± 21	0.03 ± 0.00	0.35 ± 0.00	-1.00 ± 0.00	0.09 ± 0.71	3σ
XMM-152[t]	1:34:10.14	30:47:16.78	247 ± 56	227 ± 30	109 ± 21	78 ± 15	60 ± 19	-0.29 ± 0.33	0.17 ± 0.32	0.52 ± 0.04	0.18 ± 0.03	3σ
XMM-153	1:34:10.65	30:42:23.51	2947 ± 69	2628 ± 77	1683 ± 51	903 ± 37	184 ± 25	-0.35 ± 0.16	-0.22 ± 0.13	0.63 ± 0.01	0.32 ± 0.00	3σ
XMM-154	1:34:10.92	30:39:00.70	139 ± 25	123 ± 25	55 ± 16	49 ± 14	47 ± 19	-0.03 ± 0.30	0.43 ± 0.40	0.93 ± 0.05	0.49 ± 0.04	2σ
XMM-159	1:34:13.02	30:48:36.11	99 ± 26	64 ± 23	21 ± 11	32 ± 12	77 ± 21	0.21 ± 0.41	-0.17 ± 0.45	–	–	<
XMM-160	1:34:13.65	30:43:27.01	98 ± 21	58 ± 20	57 ± 16	25 ± 10	18 ± 13	0.04 ± 0.41	0.08 ± 0.46	–	–	3σ
XMM-161	1:34:13.71	30:48:17.47	106 ± 24	57 ± 20	17 ± 13	37 ± 11	52 ± 17	0.09 ± 0.49	-0.13 ± 0.47	–	–	2σ
XMM-163	1:34:14.10	30:34:30.92	70 ± 23	60 ± 21	36 ± 14	20 ± 11	11 ± 16	-0.36 ± 0.31	0.10 ± 0.31	–	–	<
XMM-165	1:34:14.37	30:53:52.65	301 ± 38	255 ± 27	99 ± 17	144 ± 17	41 ± 15	0.10 ± 0.33	-0.20 ± 0.35	0.36 ± 0.03	-0.19 ± 0.02	3σ
XMM-166	1:34:14.38	30:39:41.56	132 ± 34	89 ± 23	46 ± 15	57 ± 14	15 ± 12	-0.30 ± 0.30	-0.08 ± 0.24	–	–	2σ
XMM-168	1:34:14.67	30:31:50.92	76 ± 26	53 ± 19	22 ± 11	40 ± 12	20 ± 12	0.49 ± 0.33	-0.47 ± 0.36	–	–	2σ
XMM-169	1:34:15.69	30:33:00.67	279 ± 31	276 ± 31	157 ± 22	106 ± 17	48 ± 18	-0.03 ± 0.49	0.09 ± 0.48	0.48 ± 0.03	-0.01 ± 0.03	3σ
XMM-170	1:34:16.31	30:52:32.74	109 ± 23	80 ± 22	67 ± 16	25 ± 11	20 ± 14	-0.10 ± 0.46	0.15 ± 0.47	–	–	<
XMM-171	1:34:16.46	30:33:55.07	182 ± 30	167 ± 29	67 ± 19	55 ± 15	48 ± 21	0.32 ± 0.28	-0.13 ± 0.40	0.46 ± 0.05	-0.21 ± 0.05	2σ
XMM-173	1:34:17.50	30:41:22.64	436 ± 44	368 ± 32	199 ± 22	129 ± 18	68 ± 20	-0.20 ± 0.36	-0.00 ± 0.37	0.39 ± 0.02	-0.44 ± 0.02	3σ
XMM-176	1:34:19.45	30:52:48.89	91 ± 25	57 ± 20	1 ± 10	31 ± 11	44 ± 16	-0.06 ± 0.41	0.21 ± 0.48	–	–	–

ID	RA	Dec	0.2-2.0 keV Cts	0.35-2.0 keV Cts	0.3-0.7 keV Cts	0.7-1.1 keV Cts	1.1-4.2 keV Cts	HR1	HR2	$HR1_{XMM}$	$HR2_{XMM}$	L10 Detect
XMM-179	1:34:22.94	30:54:22.95	172 ± 28	185 ± 26	73 ± 16	53 ± 13	59 ± 19	-0.27 ± 0.39	0.19 ± 0.38	0.44 ± 0.03	-0.83 ± 0.04	3σ
XMM-180	1:34:23.34	30:25:26.85	152 ± 22	150 ± 22	43 ± 12	62 ± 12	71 ± 19	-0.13 ± 0.40	-0.10 ± 0.33	0.67 ± 0.07	0.42 ± 0.03	2σ
XMM-183	1:34:25.40	30:54:57.44	110 ± 23	86 ± 22	24 ± 11	33 ± 12	62 ± 20	0.02 ± 0.33	0.31 ± 0.45	0.50 ± 0.30	0.74 ± 0.07	3σ
XMM-185	1:34:25.82	30:33:17.02	342 ± 31	353 ± 30	43 ± 13	111 ± 16	272 ± 27	-0.09 ± 0.45	0.20 ± 0.48	0.69 ± 0.05	0.38 ± 0.02	3σ
XMM-187[t]	1:34:30.22	30:35:10.51	163 ± 46	52 ± 20	20 ± 11	10 ± 8	132 ± 26	-0.06 ± 0.40	0.18 ± 0.50	0.39 ± 0.04	-0.35 ± 0.04	–
XMM-188	1:34:30.29	30:35:44.80	119 ± 26	88 ± 24	52 ± 15	35 ± 12	26 ± 16	0.12 ± 0.50	-0.14 ± 0.49	–	–	2σ
XMM-189	1:34:30.93	30:56:39.82	164 ± 22	141 ± 22	87 ± 15	48 ± 11	20 ± 12	-0.01 ± 0.37	0.20 ± 0.50	0.55 ± 0.04	0.04 ± 0.03	2σ
XMM-190	1:34:32.63	30:35:30.37	154 ± 25	138 ± 26	61 ± 17	42 ± 13	53 ± 19	0.04 ± 0.44	0.06 ± 0.53	0.44 ± 0.05	0.16 ± 0.04	<
XMM-192	1:34:35.52	30:52:10.97	130 ± 23	106 ± 21	91 ± 17	46 ± 14	29 ± 16	-0.15 ± 0.44	0.15 ± 0.42	0.57 ± 0.05	0.15 ± 0.04	3σ
XMM-195	1:34:38.73	30:37:56.82	90 ± 23	66 ± 20	25 ± 12	34 ± 12	76 ± 20	-0.03 ± 0.38	0.21 ± 0.48	0.87 ± 0.09	0.41 ± 0.04	<
XMM-198	1:34:40.74	30:43:36.44	62 ± 20	19 ± 18	17 ± 14	16 ± 11	27 ± 13	-0.00 ± 0.40	0.24 ± 0.51	–	–	3σ
XMM-199	1:34:41.09	30:43:26.33	669 ± 36	668 ± 37	402 ± 27	224 ± 20	17 ± 12	-0.05 ± 0.37	0.27 ± 0.48	0.57 ± 0.02	-0.12 ± 0.02	3σ

[e] Unrealistic source count errors from `emldetect` in at least one individual band. Source count errors pegged to total count values.

[t] Total counts in the full band are discrepant by a factor of two from the summation of counts in each individual band due an `emldetect` merging issue. Total counts in the 0.2-2.0 keV band are reported as the sum of counts in the 0.2-0.5 keV, 0.5-1.0 keV, and 1.0-2.0 keV band.

at the 2σ level in the 0.35-2.0 keV band on the size scale of SNRs in the *XMM-Newton* imaging.

We have also inspected all measurements at the locations of SNR candidates by eye to validate the detections and non-detections in our sample. In some cases, overlapping sources in the *XMM-Newton* data lead to erroneously high fluxes for a single SNR candidate. For these sources, if there is a previous X-ray detection of the SNR (i.e. from L10), the source is flagged as contaminated by the overlapping source ('c'), and the measured flux is likely too high and thus treated as an upper limit. If there is a nearby contaminating X-ray source, but no previous X-ray detection at the location of the SNR candidate, the source is denoted with the 'x' flag, and the flux is treated as an upper limit, and the source a non-detection. Those sources that did not appear to be reliable detections in the by-eye validation are denoted by the 'n' flag, and their fluxes are also reported as upper limits, and the sources treated as non-detections. As noted in Section 2.1 sources marked 't' have full band totals that come from the sum of the individual band runs from `emldetect`. Sources with erroneous `emldetect` count errors in at least one band are denoted by the 'e' flag, and their count errors are pegged to the total number of counts in that band.

All 218 sources are recorded in Table **??**. We report ID numbers in this catalog, corresponding ID numbers in both L10 and LL14, *XMM-Newton* positions, counts in the 0.2-2.0 keV band, count rates and associated errors in the 0.2-2.0 keV band in s^{-1}, fluxes from `elmdetect` (sum of all EPIC instruments) in the 0.2-2.0 keV band in ergs cm^{-2} s^{-1} (used for detection), fluxes in the 0.35-2.0 keV band in ergs cm^{-2} s^{-1} (used for comparison to L10), SNR sizes (in pc) from L10 and LL14, [SII]/Hα from both L10 and LL14, and the log of Hα luminosity in ergs s^{-1} from both L10 and LL14. Individual source ID numbers are denoted with the 'c', 'x', 'n', 't', and 'e' flags as described above. Sources that are upper limit measurements in this survey have fluxes preceded by <.

In addition to listing all 218 sources in Table **??**, we also list all 3σ detections only in Table **??**, along with their associated counts (sum of all EPIC instruments) and count errors in the 0.2-2.0 keV, 0.35-2.0 keV, 0.3-0.7 keV, 0.7-1.1 keV, and 1.1-4.2 keV bands. The last three bands are used to compute HRs for all detected sources only as described in Section 3.4. The HRs in these bands, computed with counts using the Bayesian Estimation of Hardness Ratios (BEHR) method Park et al. (2006), are listed with their associated errors in columns 9-10 of Table **??**. Columns 11-12 similarly list the HRs and associated errors calculated from the 0.2-0.5 keV, 0.5-1.0 keV, and 1.0-2.0 keV bands using BEHR. The final column of Table **??** denotes the level at which the source was measured in the 0.35-2.0 keV band in L10: < for upper limit, 2σ, or 3σ. The comparison of this catalog with those of L10 and LL14 is described below.

The vast majority of extragalactic SNRs, including those in M33, were first identified optically based on elevated [SII]/Hα ratios as compared to HII regions. This technique works well in general, especially for brighter objects, but HII contamination for fainter objects, especially in complex regions, can affect the observed [SII]/Hα ratio and cause uncertainty in some optical identifications. We therefore view 3σ X-ray detection of a previously optically identified SNR to be a strong confirmation of SNR detection based on both the elevated [SII]/Hα as well as strong X-ray emission. Of course, some of the optically identified SNR candidates that are undetected in X-rays may simply fall below our detection threshold and thus still be SNR detections. However, for the reasons described here, and in Section 3.1, we consider sources that are identified optically as well as measured at 3σ confidence in X-rays to be well-confirmed SNRs. These sources, and those detected in X-rays at the 3σ level from L10, are regarded as X-ray confirmed SNRs in all subsequent detectability analyses, while any candidates measured less than 3σ are considered non-detections in the analysis that follows.

We cross-correlate all our SNR candidates with measurements from LL14 and L10 to determine the number of newly X-ray detected SNRs in this catalog. The position of each of the 137 L10 sources was inspected by eye for a counterpart not already known to be a point source in the W15 catalog. To cross-correlate with LL14, we searched for counterparts in the W15 catalog out to a maximum separation of 10" for those sources not already matched to sources in L10. This resulted in 69 matches of the 78 newly reported sources in LL14. The remainder of the LL14 sources (121) were previously matched to counterparts in L10. For those sources in both L10 and LL14 that did not have a counterpart in W15 after cross-correlation we forced `emldetect` to make measurements at the locations of these sources to ensure that we would measure upper limits for all sources.

Although LL14 report 79 new SNR candidates over previous works, we find one of these 79 sources to have a potential counterpart in L10 (XMM-189, L10-122, LL14-174). As a result, our census of SNR candidates totals 218: 137 from L10, 78 from LL14, and three from W15. From our measurements of the locations of these SNRs we detect 105 at 3σ confidence and 145 at 2σ confidence. We measure upper-limits for the remaining 73 non-detections. Of our 105 3σ detections, 54 are newly detected in X-rays at 3σ, 3 are newly discovered in X-rays from this data set, 48 are 3σ detections in both L10 and this work, and 96 are reported in LL14. There are six SNRs that were detected in L10 but are not detected here. Of the six L10 detections that are undetected here, the majority have between 2-8 times more exposure in the ChASeM33 survey due to overlapping observations than the exposure times from W15. The other sources are on regions of the detector that are unfavorable to detection i.e. far off-axis, or near a chip gap on the detector. There are 25 SNRs which are upper limits in both L10 and this work. Of the 78 SNR candidates in LL14 and not in L10, we measure 18 as 3σ detections, 39 at 2σ confidence, and the remaining 39 as upper limits. In general, we are less likely to detect in X-rays the SNR candidates newly reported in LL14 compared to those SNR candidates reported in both L10 and LL14. This is very likely because the new LL14 objects have a lower mean surface brightness than the SNRs previously reported in L10, indicating that they are older and/or interacting with less dense ISM, both of which tend toward lower expected X-ray emission.

The three newly discovered SNRs were first reported in W15. The brightest of these is denoted as XMM-034 here. This SNR (source 383 in W15) is now the fifth brightest X-ray emitting SNR in M33 with a 0.35-2 keV flux of 2.77×10^{-14} erg cm^{-2} s^{-1} (L_X(0.35-2.0 keV) = 2.2×10^{36} erg s^{-1}). The discovery of these new SNRs was facilitated by the larger survey area and increased soft sensitivity of *XMM-Newton*. In particular, any source that had strong emission below 1 keV compared to above 1 keV and was not already classified as an SNR was studied in the [S II] and Hα images of Massey et al. (2006) to see if the region hosted an SNR. This method for SNR candidate detection is discussed in more detail in W15.

We provide an updated Venn diagram of the current multi-wavelength detections of SNRs in M33 in Figure 1. The prevalence of optically detected SNRs with elevated [SII]/Hα is due primarily to the the efficacy of this diagnostic ratio in separating SNRs from other contaminants. We boost the number of X-ray detections for

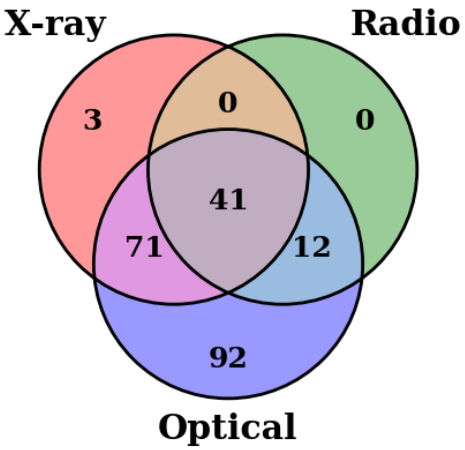

Figure 1. Venn diagram of the current multi-wavelength sample of SNRs in M33. Optical detections are based on elevated [SII]/Hα ratios and come from the catalogs of L10 and LL14. X-ray detections are from this work and the work of L10. Radio detections are taken from Gordon et al. (1999).

the previously optically detected sources owing to our large survey area and increased soft sensitivity, which is particularly adept at detecting thermal X-ray emission of extended sources. The lack of SNRs detected only in X-rays is due to the difficulty in separating SNR candidates from other sources of soft X-ray emission on the basis of X-rays alone. By selecting primarily for candidates with multiwavelength confirmation (optical and X-ray), we may be missing some young, X-ray emitting SNRs in the free expansion phase. The dearth of radio detected SNRs is affected by observational limits; most radio surveys do not furnish the requisite angular resolution and sensitivity to definitively identify SNRs without optical or X-ray follow-up. In the absence of a deep radio survey of M33, the combination of optical emission-line diagnostics and X-ray detections remains the most reliable way to identify SNRs, although such detection methods may be biased against detecting SNRs hosting pulsar wind nebulae (plerion-type SNRs), SNRs that are Balmer-dominated, and oxygen-rich SNRs.

3.2 Spectral Fitting

We attempt to type the progenitors for 15 of the SNRs in our sample by fitting their spectra using `XSPEC`. These 15 sources are some of the brightest X-ray emitting SNRs in M33 for which there is both *XMM-Newton* and *Chandra* data, and for which there are enough on-axis counts for detailed spectral fitting. We used both *XMM-Newton* and *Chandra* data in cases where *Chandra* data was available and provided $\approx$ 40% more counts than *XMM-Newton* data alone (11 SNRs). All remaining SNRs were fit using *XMM-Newton* data only (four). For each of these SNRs we perform a simultaneous fit to both the unbinned source and background components. While this method for fitting is more computationally expensive than one in which the background is directly subtracted from the source spectrum before fitting, it avoids the problems with the non-Poisson nature of background-subtracted data and makes optimal use of the full spectral information of the SNRs. We describe the individual source and background models and fitting method in the following sections. For more details on how the spectral extractions themselves were carried out, see the Appendix.

3.2.1 *Background Model*

Our background spectra were fitted with a two component model: a sky component, plus a detector component. The blank sky background was modeled as a pair of absorbed thermal plasma components (`TBabs`, $N_H = 5{\times}10^{20}$ cm^{-2}). The best-fit low-T component had kT= 0.16 keV, and the higher temperature component had kT= 0.75 keV. When fitting the SNRs, all blank sky background parameters were frozen, except for an overall multiplicative constant factor which was allowed to vary for all instruments.

For the pn, the detector component was modeled as a broad (σ = 0.455 keV) Gaussian at 0 keV and a broken power-law. In addition, Gaussian components were added for the detector fluorescence lines near 1.49 keV (Al-Kα), 2.15 keV (Au-L complex), 5.4 keV (Cr-Kα), 5.9 keV (Mn-Kα), 6.4 keV (Fe-Kα), 7.47 keV (Ni-Kα), 8.04 keV (Cu-Kα), 8.62 keV (Zn-Kα), and 9.6 keV (Zn-Kβ). For the MOS1 and MOS2 detectors, the model consists of a pair of broken power-laws to model the continuum component. The fluorescence lines listed above were added, along with a line at 1.75 keV (Si-Kα). The detector plus blank sky background models were fit to spectra covering most of each detector with point sources removed. The detector fluorescence line energies were fitted, and the line widths allowed to vary. Finally, the line energies and widths were all frozen, and the normalizations were all tied to appropriate multiples of an overall multiplicative constant factor, one for each detector background model. In subsequent fitting, only the multiplicative constant was allowed to vary.

Thus, the complete background model spectra have a scaling factor for the blank sky component, and separate scaling factors for each of the MOS1, MOS2, pn, and ACIS detector models. The background spectra are fit first with this model, and the results of this fit are supplied as inputs for the background component of the subsequent total (source + background) fit. This method thus accounts for the background while performing fits to the source spectra, as opposed to subtracting any signal from the source data before fitting, which preserves the Poisson characteristics of the data and provides more reliable estimates of the contribution of the background.

3.2.2 *Simultaneous Fitting of Chandra and XMM*

We fit both the *Chandra* and *XMM-Newton* data simultaneously for 11 SNRs. The fits were carried out using `XSPEC` with a plane-parallel shock model (`vpshock`) (Borkowski et al. 2001). All parameters in the `vpshock` model were tied between all instruments. In the `vpshock` model the individual abundances of O, Ne, Mg, Si and Fe are allowed to vary for SNRs with a large enough number of spectral counts with all other abundances (aside from H and He) frozen to values of 0.5. The Galactic absorption was fixed using a `tbabs` model to a value of 0.5×10^{21} cm^{-2} (Wilms et al. 2000), while the absorption in M33 was allowed to vary using a `tbvarabs` model; the metallicity for absorption in M33 was fixed at 0.5 times solar. The spectra were fit with unbinned channels and the C statistic was used. The absorption, shock temperatures, individual abundances, and ionization timescales were allowed to vary in the `vpshock` model. The remaining 4 SNRs did not have a significant contribution from the *Chandra* data to their total spectral counts, and thus were fit using *XMM-Newton* data only, though using the same model as above.

Table 4. Parameters from XSPEC fits for 15 SNRs in our sample with detailed spectral fits. Column 1: source ID number in this catalog. Column 2: source counts in the 0.35-2.0 keV band. Column 3: hydrogen column density for M33 from tbvarabs model. Column 4: plasma temperature from the vpshock model. Column 5: the ionization timescale from the vpshock model. Column 6: the normalization from the vpshock model. Columns 7-11: the elemental abundances from the vpshock model listed with respect to solar values. All units are given in the column headers.

ID	0.35-2.0 keV Cts	N_H 10^{22} cm^{-2}	kT_e keV	τ 10^{11} cm^{-3} s	K 10^{-4} cm^{-5}	O	Ne	Mg	Si	Fe
XMM-041	11878	$0.02^{+0.06}_{-0.02}$	$0.66^{+0.03}_{-0.02}$	$3.48^{+0.87}_{-1.02}$	> 0.18	$0.51^{+0.12}_{-0.15}$	$0.56^{+0.08}_{-0.10}$	$0.47^{+0.08}_{-0.10}$	$0.56^{+0.15}_{-0.12}$	$0.45^{+0.06}_{-0.08}$
XMM-073	4347	$0.21^{+0.12}_{-0.11}$	$0.69^{+0.21}_{-0.17}$	$1.35^{+0.80}_{-0.45}$	$0.39^{+0.56}_{-0.14}$	$0.34^{+0.15}_{-0.13}$	$0.33^{+0.07}_{-0.06}$	$0.86^{+0.21}_{-0.15}$	$0.50^{+0.25}_{-0.18}$	$0.27^{+0.22}_{-0.06}$
XMM-119	2665	$0.10^{+0.01}_{-0.10}$	$0.56^{+0.13}_{-0.08}$	$1.56^{+1.12}_{-0.88}$	$0.42^{+0.13}_{-0.15}$	$0.20^{+0.04}_{-0.03}$	$0.31^{+0.08}_{-0.05}$	$0.25^{+0.13}_{-0.08}$	$0.48^{+0.33}_{-0.22}$	$0.20^{+0.13}_{-0.03}$
XMM-067	2109	$0.11^{+0.19}_{-0.11}$	$0.54^{+0.05}_{-0.18}$	$7.73^{+5.27}_{-4.31}$	$0.34^{+0.59}_{-0.14}$	$0.27^{+0.17}_{-0.13}$	$0.40^{+0.19}_{-0.19}$	$0.19^{+0.2}_{-0.15}$	$0.48^{+0.52}_{-0.36}$	$0.18^{+0.07}_{-0.10}$
XMM-153	1910	$0.10^{+0.04}_{-0.10}$	$0.74^{+0.22}_{-0.23}$	$0.46^{+0.85}_{-0.23}$	$0.15^{+0.12}_{-0.05}$	$0.26^{+0.05}_{-0.07}$	$0.31^{+0.09}_{-0.11}$	$0.17^{+0.17}_{-0.14}$	$0.85^{+0.45}_{-0.50}$	$0.34^{+0.16}_{-0.17}$
XMM-068	1207	$0.00^{+0.03}_{-0.00}$	$0.48^{+0.09}_{-0.03}$	$5.62^{+8.38}_{-1.85}$	$0.23^{+0.04}_{-0.07}$	$0.43^{+0.19}_{-0.07}$	$0.57^{+0.21}_{-0.12}$	$0.36^{+0.12}_{-0.21}$	$0.39^{+0.51}_{-0.38}$	$0.15^{+0.03}_{-0.03}$
XMM-034	742	$0.10^{+0.06}_{-0.10}$	$0.65^{+0.89}_{-0.16}$	$0.27^{+0.38}_{-0.12}$	$0.03^{+0.02}_{-0.01}$	$0.67^{+0.19}_{-0.15}$	–	–	–	$0.36^{+0.33}_{-0.21}$
XMM-039	1820	$0.10^{+0.13}_{-0.10}$	$0.51^{+0.21}_{-0.18}$	$0.9^{+2.43}_{-0.52}$	> 0.03	$0.39^{+0.19}_{-0.13}$	$0.57^{+0.26}_{-0.24}$	$0.41^{+0.50}_{-0.30}$	$0.42^{+1.04}_{-0.42}$	$0.29^{+0.24}_{-0.14}$
XMM-082	2143	<0.14	$0.43^{+0.01}_{-0.03}$	>50.00	$0.14^{+0.08}_{-0.10}$	$0.20^{+0.23}_{-0.03}$	$0.40^{+0.13}_{-0.07}$	$0.70^{+0.08}_{-0.18}$	$0.36^{+0.29}_{-0.25}$	$0.10^{+0.02}_{-0.02}$
XMM-151	937	$0.10^{+0.04}_{-0.10}$	$0.36^{+0.24}_{-0.14}$	$1.04^{+1.13}_{-0.03}$	>0.39	$0.48^{+0.23}_{-0.14}$	–	–	–	$0.50^{+0.32}_{-0.22}$
XMM-066	982	$0.26^{+0.00}_{-0.01}$	$0.6^{+0.03}_{-0.4}$	$0.17^{+0.07}_{-0.01}$	>0.37	$0.54^{+0.06}_{-0.13}$	–	–	–	$1.20^{+1.17}_{-0.64}$
XMM-132	1070	$0.10^{+0.04}_{-0.10}$	$0.73^{+0.59}_{-0.28}$	$0.25^{+0.34}_{-0.15}$	>0.06	$0.64^{+0.24}_{-0.11}$	–	–	–	$0.60^{+0.53}_{-0.27}$
XMM-065	502	$0.28^{+0.31}_{-0.19}$	$0.92^{+1.59}_{-0.56}$	$0.14^{+0.21}_{-0.06}$	$0.03^{+-0.02}_{-0.01}$	–	–	–	–	–
XMM-136	585	$0.10^{+0.05}_{-0.10}$	$0.38^{+0.05}_{-0.07}$	>6.72	>0.09	$0.24^{+0.07}_{-0.13}$	–	–	–	$0.15^{+0.08}_{-0.07}$
XMM-118	310	$0.10^{+0.14}_{-0.10}$	$0.31^{+0.32}_{-0.07}$	>19.78	$0.04^{+0.03}_{-0.03}$	$0.56^{+0.77}_{-0.36}$	–	–	–	$0.31^{+0.3}_{-0.17}$

Each SNR was visually inspected prior to fitting to determine the number of useful spectral counts available for fitting. This involved examining SNR images, and removing fields in which spectral extraction regions fell on chip gaps or were far off axis. We find that > 300 useful counts are necessary for a reliable fit, while > 1200 counts are required to fit for individual abundances in a given SNR's spectrum. For the SNRs that had between 300–1200 counts, the individual abundances were frozen when performing the fit, or, O and Fe were allowed to vary, with all other abundances tied to O.

We provide the best-fitting spectral parameters and associated 90% confidence intervals from all of our fits in Table 4. The analysis of the spectral fitting results are discussed in the following section.

3.3 Spectral Fit Parameters

The parameters from the detailed spectral fitting are recorded in Table 4 for the model described in Section 3.2.2. The fitted parameters include the hydrogen column density (N_H), the electron temperature (kT_e), the ionization timescale (τ), and the normalization (K). The abundances of O, Ne, Mg, Si and Fe are reported relative to the solar value, and are allowed to vary for SNRs with > 1200 counts. An example of the model fit to the data for a single SNR (XMM-041, L10-025) is plotted in Figure 2. Each set of two panels illustrates the total fit, associated components (left panel), and the background fit only (right panel) for each instrument (pn, MOS1, MOS2, and ACIS). Figure 2 demonstrates the robustness of the fitting technique by illustrating the strong contribution of the background component, and in particular the instrument background, at higher energies.

Along with the fitted parameters we derive inferred physical parameters from these values, such as pre-shock H density (n_o), ionization age (t_{ion}), dynamical age (t_{dyn}), shock velocity (v_s), initial explosion energy (E_o), and swept-up mass (M_{su}). These parameters are calculated based on a Sedov model, and assuming a volume-filling factor of one, spherically symmetric SNRs, strong shock jump conditions, and electron-ion equilibrium. The effects of some of these simplifying assumptions are discussed in the following paragraphs. The values for the above calculated physical parameters are reported for each SNR in Table 5 and represent spatially averaged quantities over the SNR. The XSPEC model fits provide estimates for the electron temperature (kT_e), the ionization timescale (τ), and the normalization (K) (see Table 4).

Following Hughes et al. (1998) and Gaetz et al. (2007) we can calculate the Sedov model parameters in Table 5 based on the observational values for the electron temperature, ionization timescale, normalization, and SNR radii. We use the radius for each SNR reported from L10 in our calculations (see Table **??**), and assume errors of ∼ 9% on the reported radii, based on adding in quadrature an error of 5% in angular size and assuming azimuthal asymmetry, and an error of 7% in the assumed distance to M33. Errors on the derived physical quantities are calculated from the 90% confidence interval on the fitted parameters using 10,000 Monte Carlo draws from the error distribution, and the propagation of the previously stated errors on the radii and angular sizes of the SNRs.

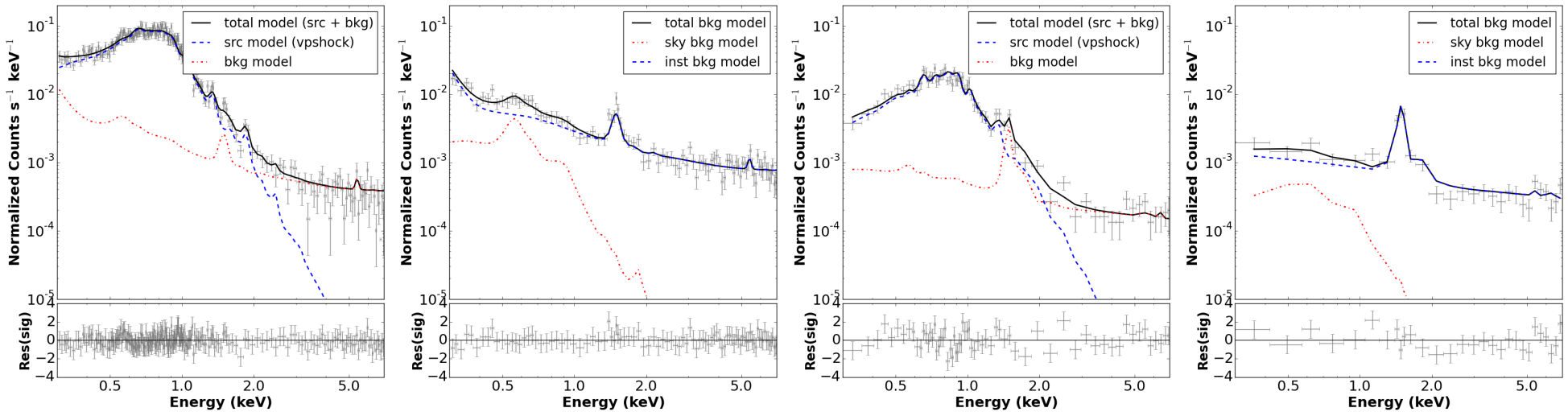

(a) pn

(b) MOS1

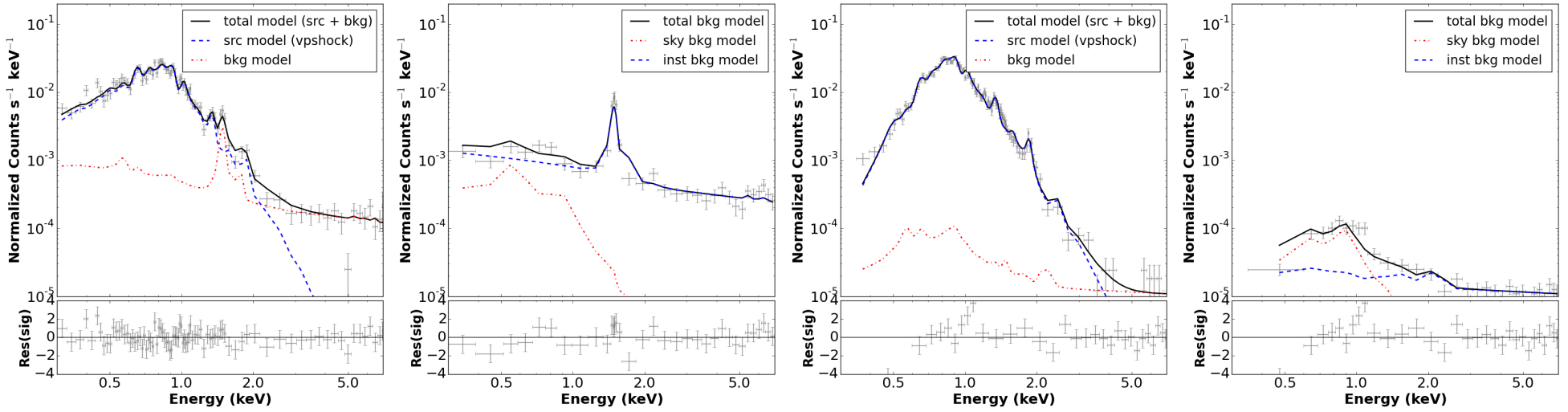

(c) MOS2

(d) ACIS

Figure 2. Sample fit for the SNR XMM-041 (L10-025) using a `vpshock` model for the source with O, Ne, Mg, Si and Fe abundances as free parameters. Panels a, b, c, and d represent fits the individual cameras: pn, MOS1, MOS2, and ACIS, respectively. Within each panel, the left-hand panel depicts the total fitted model in black, with the total model components, source (`vpshock`) and background shown in blue and red, respectively. The gray points show the data and residuals with associated errorbars. The right-hand panel shows the total fitted background model in black, and its components, sky and instrument background, in blue and red. The data and residuals are again plotted as gray points, with associated errorbars.

The pre-shock H density is calculated from the fitted normalization, distance to M33, and measured radii using the following equation from Gaetz et al. (2007):

$$n_o = 1.58 K_{-4}^{1/2} D_{800} R_{s,10}^{3/2} \ cm^{-3} \quad (1)$$

where K_{-4} is the normalization in units of 10^{-4} cm^{-5}, D_{800} is the assumed distance in units of 800 kpc, and $R_{s,10}$ is the source radius in units of 10 pc. Assuming strong shock jump conditions, this pre-shock H density can be used to calculate the post-shock density as follows: $n_e = 4.8 \times n_o$. The post-shock density, coupled with the ionization timescale (τ) gives an estimate of the ionization age. Following Borkowski et al. (2001), we note that at a given shock velocity the ionization timescale, τ, from a plane-parallel shock model, such as the `vpshock` model used in our fits, may be considerably larger than the emission-averaged ionization timescale, $<\tau>$, in the Sedov model. We calculate the ionization ages in Table 5 from the plane-parallel shock τ, and note that the ages based on the Sedov $<\tau>$ may be smaller, leading the ages reported in Table 5 to be an upper limit. The dynamical ages are proportional to the observed radii divided by the shock velocity ($v_s \sim \sqrt{kT_e}$), and we find that they are systematically much larger than the ages calculated based on the ionization timescale from the fits. This may imply that the simplifying assumptions of all SNRs in the Sedov phase and in electron-ion equilibrium as applied to our constant-temperature plane-parallel shock model fits are not appropriate for all SNRs. Despite this, we proceed with these assumptions to provide estimates of the explosion energies and swept-up masses for each fitted SNR. We derive an average explosion energy for all SNRs of $\sim 1.5 \times 10^{51}$ ergs and swept-up masses that are all on the order of hundreds M$_\odot$. There is an uncertainty in the swept-up masses due to the distribution of circumstellar and interstellar material around the progenitor that is not accounted for here. The Sedov model assumes a point explosion in a uniform medium, however for a CC SN the stellar winds of the progenitor will have sculpted the surrounding medium, meaning that the density currently being encountered by the blast wave may be larger than the density encountered at an earlier stage, leading to a general overestimate of the swept-up mass. For this reason, we consider the swept-up mass calculations to be an upper bound.

The large swept-up masses for the fitted sample imply that the majority of these SNRs are older and therefore ISM-dominated. Given the derived ages and swept-up masses, we expect the SNR ejecta to be well-mixed with the surroundings, leading to fitted abundances that more closely resemble that of their surroundings, as opposed to the ejecta distributions expected for individual Type Ia or CC SNe. Because of this, we are unable to definitively type any of the SNRs in our fitted sample. We do note, however, that one of the SNRs in this fitted sample—XMM-068 (L10-037, LL14-062)—has an elevated O/Fe value of ~ 3, which is markedly in excess of the O/Fe ratios for the rest of the fitted sample as demonstrated in Figure 3. In a CC SNR, we would expect that if O is enhanced, Ne and Mg would also be enhanced. Because Ne line energies overlap Fe L-shell lines there will be some blending at the resolution of the CCD, and one might expect an elevated O/Fe value simply based on an anti-correlation between Ne and Fe. We do not see a strong anti-correlation between the fitted Ne and Fe values for this SNR based on a contour plot generated with the `XSPEC steppar` command, and further the Ne value is not overly abundant in the fit compared to the expected M33 metallicity abundance. This implies that the Fe abundance is actually deficient compared to O in this

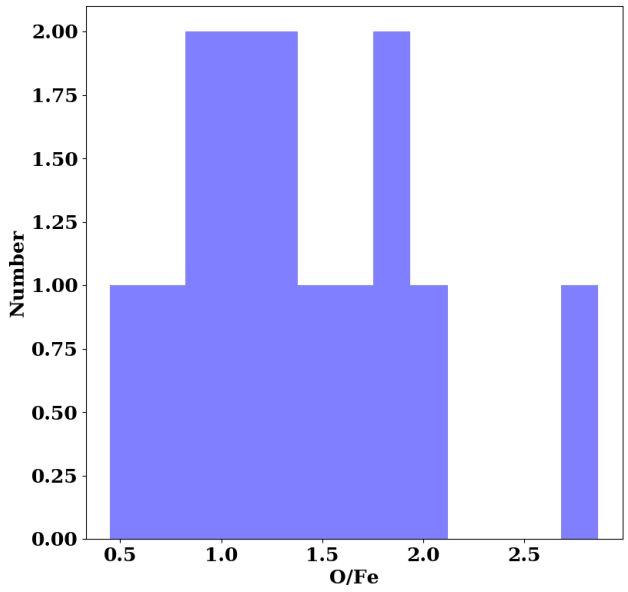

Figure 3. Histogram of the O/Fe values for all 15 fitted SNRs. There is one clear outlier (XMM-068) from the overall distribution, with highly elevated O/Fe, which may be indicative of CC ejecta enrichment in the vicinity of this SNR.

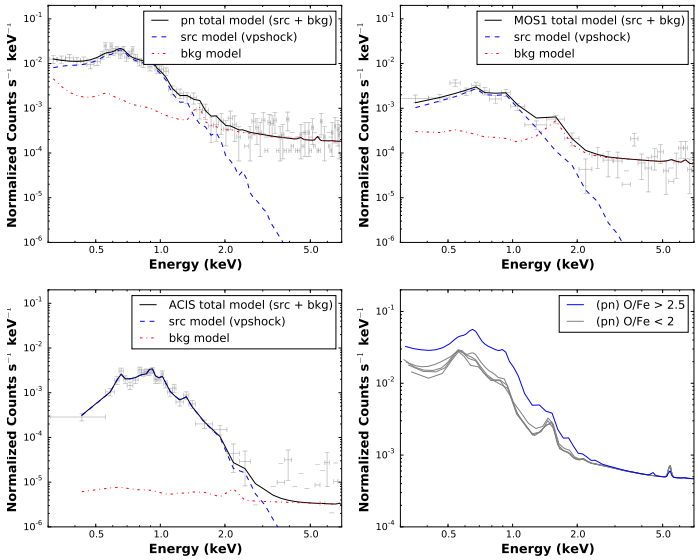

Figure 4. `XSPEC vpshock` model fit for SNR XMM-068 for the pn (top-left), MOS1 (top-right), and ACIS (bottom-left) instruments. The model components are labeled in each panel. The bottom right panel compares the fitted pn spectrum for XMM-068 to the pn spectra for four SNRs in this sample with similar numbers of counts, but lower O/Fe values. All spectra have been normalized to have the same number of counts at 5 keV.

SNR, as opposed to simply *appearing* less abundant due to being masked by an enhanced Ne abundance based on lines at energies similar to those of the Fe L-shell lines which are not resolved at CCD resolution. We plot the spectral fit results for this SNR in Figure 4 for the pn, MOS1, and ACIS instruments, as well as for the pn compared to four other pn spectra for SNRs with O/Fe < 2 (bottom-right panel). Qualitatively, there is no marked difference

Table 5. Physical parameters for SNRs calculated from fitted parameters in Table 4. Column 1: source ID number in this catalog. Column 2: pre-shock H density. Column 3: ionization age for the SNR. Column 4: dynamical age for the SNR. Column 5: shock velocity. Column 6: explosion energy. Column 7: swept-up mass. All units are given in the column headers.

ID	n_o cm^{-3}	t_{ion} 10^3 yrs	t_{dyn} 10^3 yrs	v_s km s^{-1}	E_o 10^{51} erg	M_{su} $M_\odot$
XMM-041	>0.40	$5.00^{+1.20}_{-5.00}$	$6.70^{+0.40}_{-0.50}$	740^{+20}_{-20}	>1.50	>180
XMM-073	$2.39^{+1.44}_{-0.57}$	$0.40^{+0.30}_{-0.20}$	$3.40^{+0.60}_{-0.50}$	760^{+110}_{-100}	$1.00^{+0.80}_{-0.40}$	120^{+80}_{-40}
XMM-119	$1.04^{+0.24}_{-0.25}$	$1.00^{+0.90}_{-0.50}$	$5.80^{+0.60}_{-0.70}$	680^{+80}_{-50}	$1.60^{+0.60}_{-0.50}$	230^{+70}_{-80}
XMM-067	$1.17^{+0.81}_{-0.30}$	$4.40^{+3.70}_{-2.70}$	$5.30^{+1.30}_{-0.40}$	670^{+30}_{-130}	$1.20^{+0.80}_{-0.50}$	180^{+140}_{-60}
XMM-153	$0.78^{+0.30}_{-0.17}$	$0.40^{+0.70}_{-0.20}$	$4.60^{+1.00}_{-0.60}$	780^{+110}_{-140}	$1.10^{+0.60}_{-0.40}$	120^{+60}_{-40}
XMM-068	$0.30^{+0.06}_{-0.07}$	$12.30^{+20.50}_{-4.10}$	$10.00^{+0.70}_{-1.00}$	630^{+60}_{-30}	$2.10^{+0.70}_{-0.60}$	350^{+100}_{-110}
XMM-034	$0.16^{+0.06}_{-0.04}$	$1.10^{+1.80}_{-0.50}$	$7.30^{+1.20}_{-2.60}$	730^{+400}_{-100}	$0.80^{+1.20}_{-0.30}$	110^{+50}_{-40}
XMM-039	>0.15	$2.70^{+6.50}_{-2.70}$	$7.60^{+1.90}_{-1.30}$	650^{+130}_{-130}	>0.40	>70
XMM-082	$0.27^{+0.09}_{-0.11}$	>103.40	$9.90^{+0.80}_{-0.60}$	600^{+10}_{-30}	$1.30^{+0.50}_{-0.60}$	250^{+100}_{-110}
XMM-151	>1.36	$0.30^{+0.5}_{-0.3}$	$7.2^{+2.0}_{-1.7}$	550^{+160}_{-120}	>1.1	>270
XMM-066	>1.02	$0.10^{+0.00}_{-0.10}$	$5.30^{+3.00}_{-0.30}$	710^{+20}_{-260}	>0.90	>180
XMM-132	>0.14	$0.90^{+1.20}_{-0.90}$	$8.70^{+2.50}_{-2.30}$	780^{+270}_{-170}	>1.40	>180
XMM-065	$0.11^{+0.03}_{-0.03}$	$0.90^{+1.50}_{-0.40}$	$7.30^{+3.90}_{-2.90}$	870^{+570}_{-310}	$1.40^{+2.60}_{-0.90}$	130^{+50}_{-50}
XMM-136	>0.18	>31.30	$11.30^{+1.40}_{-1.00}$	560^{+40}_{-60}	>1.00	>200
XMM-118	$0.29^{+0.11}_{-0.12}$	>46.20	$8.20^{+1.30}_{-2.50}$	510^{+220}_{-70}	$0.30^{+0.40}_{-0.10}$	80^{+40}_{-40}

between the high O/Fe SNR (blue line), and the rest of the sample (grey lines), though without more SNRs at higher O/Fe values it is difficult to classify based on spectral shape alone.

Based on the swept-up mass of SNR XMM-068, which is in excess of 300 $M_\odot$, we note that it is most likely ISM-dominated, but may still originate from an environment with generally more CC ejecta enrichment. Interestingly, XMM-068 is the only SNR in the fitted sample that was given a progenitor classification of Type Ia by LL14 based on the surrounding stellar population. By contrast, we see evidence that O is enriched compared to Fe, even within the errors, for XMM-068, suggesting that this SNR's environment contains relics of more high-mass, CC ejecta.

The only SNR to be designated as CC in L10 is XMM-073 (L10-039, LL14-067) based on elevated O, Ne, and Mg as compared to Fe from an X-ray spectral fit. We see only slight enhancement of O, Ne, and Mg relative to Fe in our fits for XMM-073, but L10's classification is consistent with our spectral fits within the errors on the fitted abundances. However, the light element abundance enhancements relative to iron coupled with the large swept-up mass preclude the possibility of assigning a progenitor type based on our spectral fits alone.

M33, a star-forming Scd galaxy, is expected to have a much higher fraction of CC SNe than Type Ias. Mannucci et al. (2005) report a Type Ia SNe rate of $0.17^{+0.068}_{-0.063}$ per century per 10^{10} $M_\odot$ and a CC SNe rate of $0.86^{+0.319}_{-0.306}$ per century per 10^{10} $M_\odot$. Given these rates, we expect about 17% of the SNRs in M33 to be Type Ias, or around 37 of the 218 candidates. Therefore, we expect the vast majority of our sample to be CC SNe, and in particular we would expect only ~ 2 of the sample of bright SNRs with detailed spectral fits to be of Type Ia. LL14 tentatively type XMM-068 with this designation based on the surrounding stellar population, but we find no evidence in the X-ray spectral fits to support this designations (e.g. broad Fe L-shell complexes), and in fact we find evidence of enhanced O/Fe, though this SNR is likely ISM-dominated. XMM-066 (L10-035) is the only fitted SNR for which we measure O/Fe < 0.5, but this SNR was left out of the LL14 catalog due to its low [SII]/Hα value, so it has no assigned progenitor type in that catalog, and in addition, it has an extremely high swept-up mass, implying again that it would likely not retain much of the progenitor ejecta signature.

Finally, we compared both the fitted and derived parameters to physical quantities of the SNRs such as size, luminosity, and HR measure. In doing so, we find some evidence for a correlation between the pre-shock H density and the X-ray luminosity, as can be seen in Figure 5. Variations in the density of the ISM surrounding the SNR progenitor will lead to differences in the resultant SNR X-ray luminosity, with higher luminosities expected from SNRs whose progenitors explode in denser environments, so evidence of such a relation is not unexpected assuming an ISM that is not spatially uniform. One might expect a correlation between X-ray HR, SNR temperature, and SNR size, as those SNRs that are cool, and evolved will have stronger emission in the soft band and be larger in size, while hotter SNRs will have more emission in the medium band. Only very high temperature, young SNRs will have strong hard band emission (Maggi et al. 2016).

Ultimately, we do not find any significant correlations between HR1 (M-S/(H+M+S)) and the temperatures, nor between the fitted temperatures and SNR sizes, as illustrated in Figure 6, though the

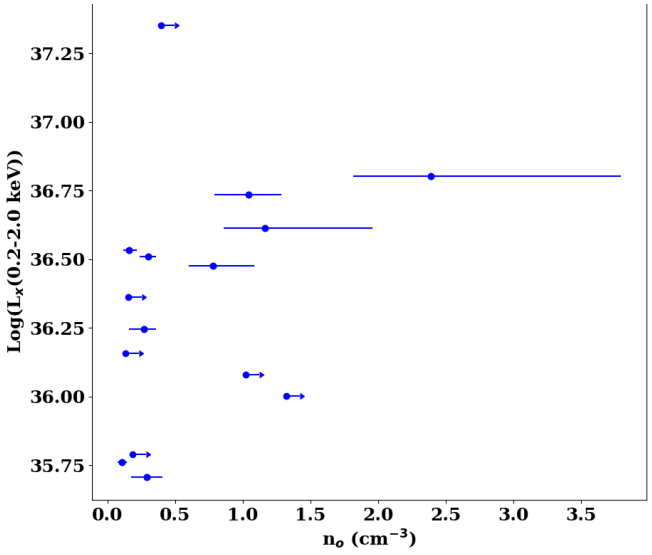

Figure 5. Pre-shock H densities derived for the 15 SNRs with spectral fits versus their X-ray luminosities in the 0.2-2.0 keV band.

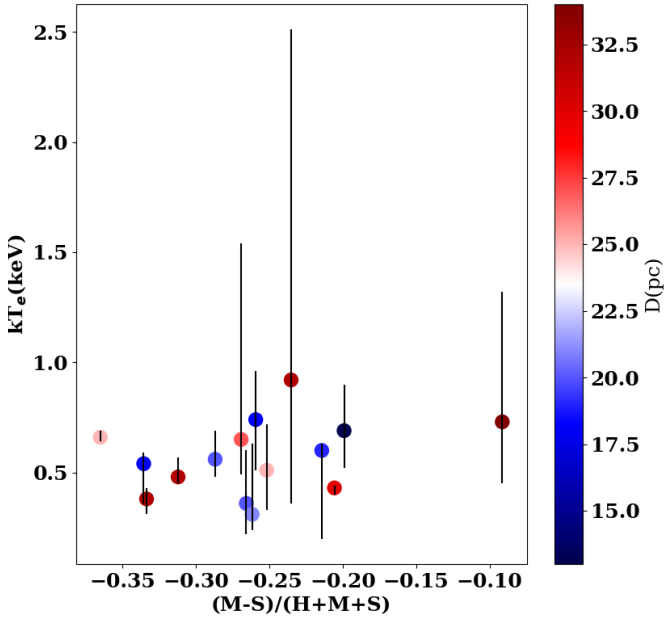

Figure 6. HR1 = (M-S)/(H+M+S), where H= 1.1-4.2 keV, M = 0.7-1.1 keV, and S = 0.3-0.7 keV versus the electron temperature from spectral fits. The points are color-coded by SNR size. We find no strong correlation between SNR temperature and HR, or SNR temperature and size.

errors on the fitted temperatures are similar to the range of measured values. Nearly all of the fitted SNRs have abundances that are similar to the M33 ISM abundance. This implies that most of the bright SNRs are ISM-dominated, and no longer display strong evidence of the ejecta signature of their progenitor. This may also indicate that fitting a global model to the entire SNR—as opposed to separately fitting and analyzing individual features—will yield fitted parameters that represent global averages of the ejecta structure of the SNR, which generally leads to some loss of information.

3.4 Hardness Ratios

Hardness ratios are often used to discriminate between X-ray source types. By comparing X-ray fluxes across different bands one may hope to isolate different spectral shapes for sources with too few counts for reliable spectral fitting. We attempted to type the sample of X-ray detected SNRs by HRs in bands defined in Maggi et al. (2014). These bands are selected to highlight specific features in a SNR's thermal spectrum. The soft band is from 0.3 keV to 0.7 keV and is dominated by oxygen lines. The medium band ranges from 0.7 keV to 1.1 keV and includes both Fe L-shell lines indicative of a Type Ia progenitor as well as Heα lines from Ne XI and Ne X, themselves indicative of a CC progenitor. The hard band goes from 1.1–4.2 keV and is comprised of thermal continuum plus lines from Mg, Si, S, Ca, and Ar. The HRs also yield valuable information in the form of temperature; hotter SNRs should exhibit harder HRs, while more evolved objects with cooler plasmas should be more evident in the soft band (Maggi et al. 2014). We calculate HRs based on counts in the soft, medium and hard bands above with the following equations:

$$HR1 = \frac{M - S}{S + M + H}, \quad HR2 = \frac{H - M}{S + M + H} \tag{2}$$

We first simulate SNR spectra in `XSPEC` using a `vpshock` model, a fixed Galactic absorption component (`tbabs`, 0.5×10^{21} cm^{-2}), and a varying M33 absorption component (`tbvarabs`). We then compute the HRs from counts in the bands defined above from the simulated SNR spectra allowing only the temperature, M33 absorption component, and abundances of O and Fe to vary, with the abundances of Ne and Mg tied to the O abundance.

The HRs computed from these simulated spectra are plotted in the top-right, bottom-left, and bottom-right panels of Figure 7. In each panel the triangular region denotes the allowed HR values for positive count measurements. The top-right panel depicts the simulated HRs for a low M33 absorption (N_H = 1×10^{20} cm^{-2}) from low temperatures (~ 0.1 keV, smaller crosses) to high temperatures (~ 1 keV, larger crosses) at a range of abundance ratios. Points are color-coded based on the abundance ratio of O/Fe: blue crosses are those SNRs with high O/Fe ratios, indicating O enrichment, grey crosses are those SNRs for which the O/Fe ratio is near unity, and red crosses are SNRs for which the O/Fe ratio is low and thus indicative Fe enrichment. The unfilled circles are the 15 SNRs for which we were able to perform detailed spectral fits (Table 4), and are also color-coded based on their fitted abundance ratios. The bottom-left panel displays the simulated HRs for an intermediate M33 absorption value (N_H = 1.2×10^{21} cm^{-2}), while the bottom-right has a high M33 absorption value (N_H = 3.5×10^{21} cm^{-2}), both with the same spread of temperatures and abundance ratios as the top-right panel. The size of the points (both simulated and fitted) indicates temperature, with smaller crosses having lower temperatures.

There is a clear trend with temperature in the simulated SNR HRs, wherein SNRs at a given O/Fe and N_H move to the left and down (softer HRs) in Figure 7 as their temperatures go from high (~ 1 keV) to low (~ 0.1 keV). This is denoted by the black arrow labeled "kT" on each panel. The progression of the panels illustrates the changes to simulated HRs with changing absorption values, with increasing absorption moving SNRs at a given temperature and abundance ratio to generally harder HRs (up and to the right). At a given temperature and value of N_H the O/Fe abundance ratio can move the HR diagonally downwards on the plot, as indicated by the black arrow labeled "O/Fe". Some separation between abundance ratios is evident in the simulated sample, with SNRs at low O/Fe

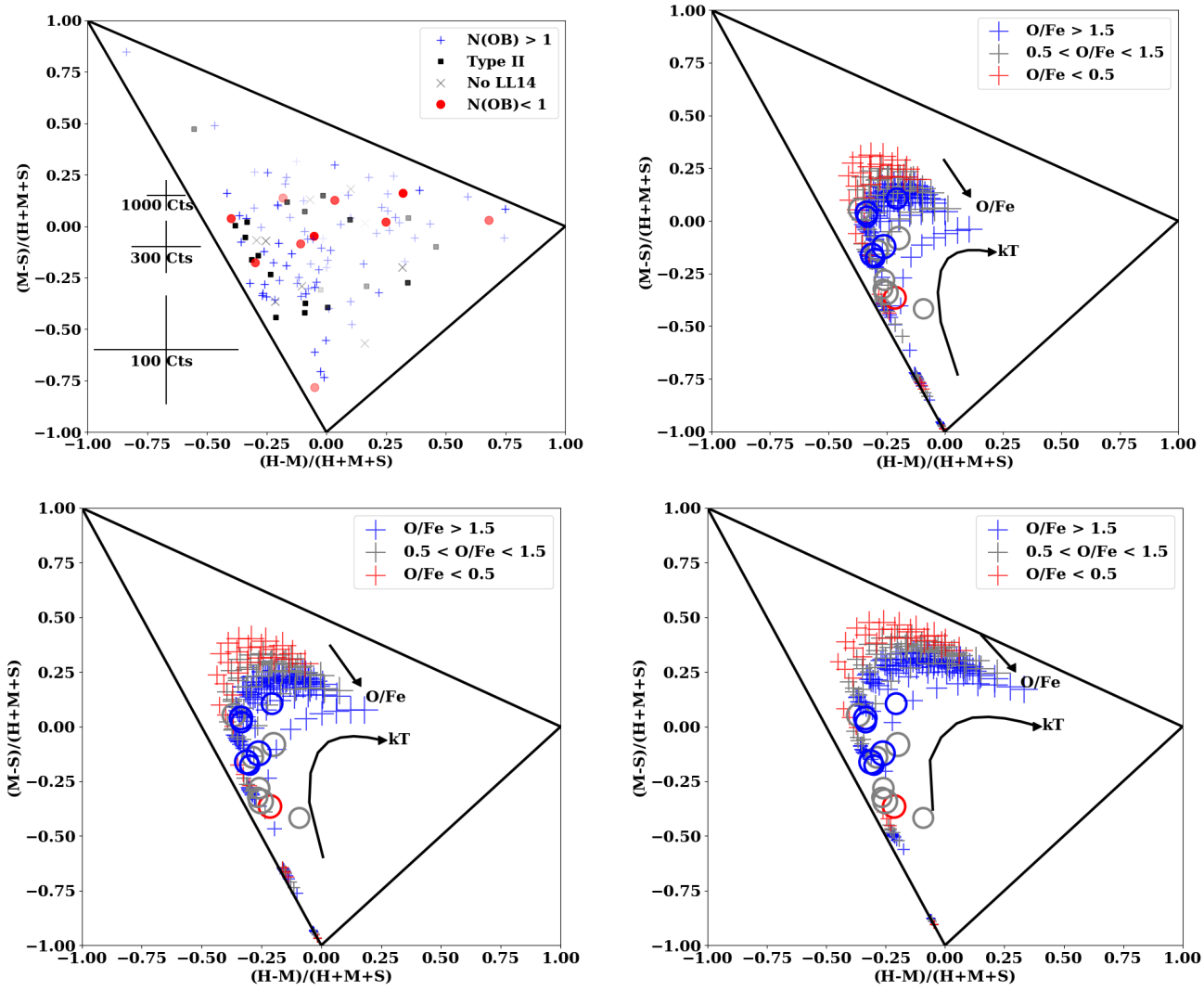

Figure 7. *Top-Left*: HR from counts in the 0.3-0.7 (soft), 0.7-1.1 (medium) and 1.1-4.2 (hard) keV bands for all SNRs detected at 3σ. Representative errors for bins of 1000 counts, 300 counts, and 100 counts are displayed for reference. Candidate Type Ia SNRs based on LL14 classifications are denoted by red circles, candidate CC SNRs from LL14 are denoted by blue crosses, and black squares are SNRs with CC progenitors based on analysis of the surrounding stellar population by Jennings et al. (2014). Those without an LL14 or Jennings et al. (2014) match are in gray. The transparency of the points is related to signal-to-noise, with the boldest points have the highest signal-to-noise values. *Top-Right*: HRs from a suite of SNR spectra simulated in `XSPEC` with a `vpshock` model and temperatures ranging from 0.1-1.0 keV, a range of O and Fe abundances, and with a fixed M33 absorption value of $N_H = 1 \times 10^{20}$ cm^{-2} (low N_H). Points are color-coded based on abundance ratio: red for low O/Fe, grey for O/Fe close to unity, and blue for elevated O/Fe. The 15 fitted SNRs are overplotted as unfilled circles using the same color scheme. The point size denotes temperature, with smaller crosses having lower temperatures. Arrows are added for reference to show the direction of increasing temperature, and increasing O/Fe ratio. *Bottom-Left:*: HRs from a suite of SNR spectra simulated in `XSPEC` with a `vpshock` model and temperatures ranging from 0.1-1.0 keV, a range of O and Fe abundances, and with a fixed M33 absorption value of $N_H = 1.2 \times 10^{21}$ cm^{-2} (intermediate N_H). *Bottom-Right:*: HRs from a suite of SNR spectra simulated in `XSPEC` with a `vpshock` model and temperatures ranging from 0.1-1.0 keV, a range of O and Fe abundances, and with a fixed M33 absorption value of $N_H = 3.5 \times 10^{21}$ cm^{-2} (high N_H). The fitted SNRs align most closely with the simulated sample at low N_H.

exhibiting larger HR1 values, possibly indicative of their stronger Fe L-shell lines and thus a Type Ia progenitor.

The fitted sample (unfilled circles) is more consistent with the simulated sample at low N_H ($N_H = 1{\times}10^{20}$ cm^{-2}) for the majority of the fitted SNRs. The only SNR with low O/Fe in our fitted sample (red unfilled circle) is roughly consistent with the simulated sample assuming a lower temperature. There is one outlier in the fitted sample that does not clearly follow any of the simulated trends. This SNR has an intermediate abundance ratio value (grey unfilled circle) and is separated from the bulk of the population with the largest HR2 value. This is source XMM-132 (L10-081, LL14-119), and is classified as a CC SNR by LL14, and by Jennings et al. (2014) with a derived progenitor mass of ~14$M_\odot$.

We next look for correlations between SNR progenitor type and HR in our sample of 3σ detections by cross-correlating our sources with those from LL14 and Jennings et al. (2014) and assigning

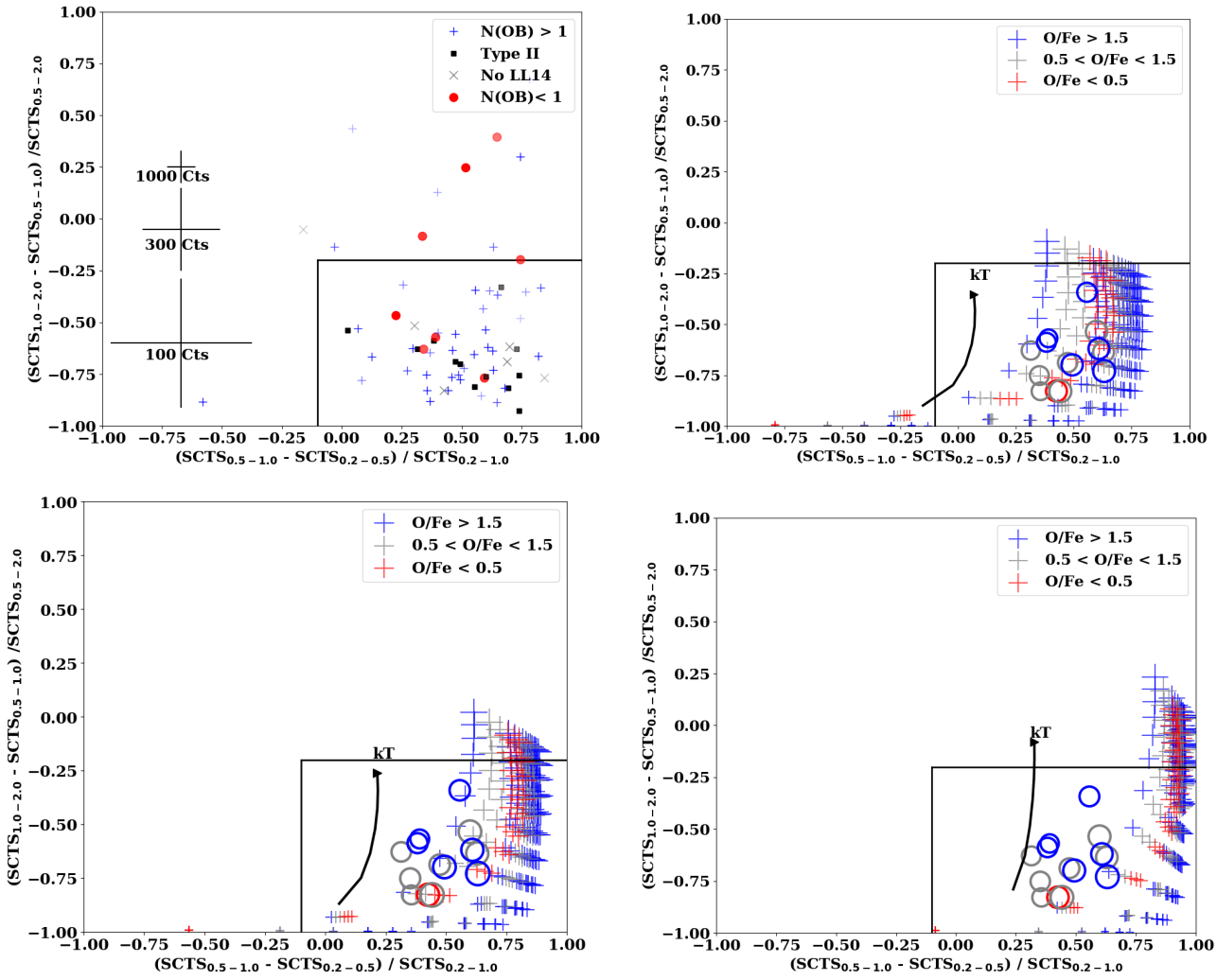

Figure 8. *Top-Left*: HR from source counts for the 0.2-0.5 (soft), 0.5-1.0 (medium) and 1.0-2.0 (hard) keV bands for SNRs detected at 3σ. Representative errors for bins of 1000 counts, 300 counts, and 100 counts are displayed for reference. Candidate Type Ia SNRs based on Lee & Lee (2014b) classifications are denoted by red circles, while the candidate CC SNRs from this same study are denoted by blue crosses. Those without a Lee & Lee (2014b) match are in gray. The majority of sources lie within the box defined by Pietsch et al. (2004) where we expect most SNRs to fall, but there is not clear separation within this between Type Ia and CC SNRs. *Top-Right*: HRs from a suite of SNR spectra simulated in `XSPEC` with a `vpshock` model and temperatures ranging from 0.1-1.0 keV, a range of O and Fe abundances, and with a fixed M33 absorption value of $N_H = 1 \times 10^{20}$ cm^{-2} (low N_H). SNRs are color-coded based on abundance ratio: red for low O/Fe, grey for O/Fe close to unity, and blue for elevated O/Fe. The 15 fitted SNRs are overplotted as unfilled circles using the same color scheme. The point size denotes temperature, with smaller crosses having lower temperatures. Arrows are added for reference to show the direction of increasing temperature. *Bottom-Left:* HRs from a suite of SNR spectra simulated in `XSPEC` with a `vpshock` model and temperatures ranging from 0.1-1.0 keV, a range of O and Fe abundances, and with a fixed M33 absorption value of $N_H = 1.2 \times 10^{21}$ cm^{-2} (intermediate N_H). *Bottom-Right:* HRs from a suite of SNR spectra simulated in `XSPEC` with a `vpshock` model and temperatures ranging from 0.1-1.0 keV, a range of O and Fe abundances, and with a fixed M33 absorption value of $N_H = 3.5 \times 10^{21}$ cm^{-2} (high N_H). The fitted SNRs align most closely with the simulated sample at low N_H, though there is no clear trend with abundance ratio and HRs in these bands.

to each SNR, when available, a possible progenitor type based on their analyses of the surrounding stellar population. We illustrate this comparison between HRs and tentative progenitor type in the top-left panel of Figure 7, with HRs and their associated errors calculated from counts in the above bands using BEHR (Park et al. 2006). Each point is color-coded based on potential progenitor type: blue crosses represent potential CC classifications (nearby OB stars found in LL14), black squares are sources with CC classification from Jennings et al. (2014), gray x's are sources for which there is no counterpart in LL14 or Jennings et al. (2014), and filled red circles are sources with potential Type Ia progenitors (no nearby OB stars found in LL14). More transparent points have lower signal-to-noise ratios. The typical HR errors for sources with 1000 counts, 300 counts, and 100 counts are displayed for reference. We find no correlation between HR in these bands and potential SNR progenitor type.

Ultimately we are far from the idealized case in the other panels of Figure 7, and the range of temperatures, column densities, and abundance ratios probed, coupled with uncertainties on the HRs, do not allow for any kind of quantitative separation for SNR progenitor

type based on HRs alone. In addition, it is perhaps not surprising to find no strong separation given that we expect only 17% of the SNRs in M33 to be of Type Ia origin (Mannucci et al. 2005), which is about 18 total out of all 3σ detections.

It is also true that some Type Ia SNRs in the Large Magellenic Cloud (LMC) are Balmer-dominated, with little to no enhancement of [SII] emission (Hughes et al. 1995). As noted by Tuohy et al. (1982) this effect arises due to a fast shock propagating into a region of neutral hydrogen and giving rise to strong Balmer emission, while [SII] emission is suppressed in the high temperature region behind the shock due to low collisional rates. This implies that we may be missing the sample of young, ejecta dominated Type Ia SNRs in M33 by selecting SNRs mainly through their enhanced [SII]/Hα ratios; however, we expect the population of young, Balmer-dominated Type Ia SNRs in particular to be quite small, as only 4 are reported in the LMC (Tuohy et al. 1982; Hughes et al. 1995; Ghavamian et al. 2007; Maggi et al. 2016). For older SNRs, the ejecta will be well-mixed with the surrounding circumstellar material, so evidence of the progenitor's ejecta signature would be diluted or erased.

In addition to the bands defined by Maggi et al. (2014) we also test the correlation between potential SNR progenitor type (derived from LL14) and HRs based on counts in the $<$ 2 keV bands. This particular set of HRs was developed to take advantage of the soft-sensitivity of *XMM-Newton*. The ratios are calculated as follows:

$$\begin{aligned} HR1_{XMM} &= (M_{XMM} - S_{XMM})/(M_{XMM} + S_{XMM}) \\ HR2_{XMM} &= (H_{XMM} - M_{XMM})/(H_{XMM} + M_{XMM}) \end{aligned} \quad (3)$$

Here, the soft band is defined as 0.2-0.5 keV, the medium band is 0.5-1 keV, and the hard band is 1.0-2.0 keV. As outlined in W15 we used these HRs to isolate new SNR candidates based on the HR cuts described by Pietsch et al. (2004), which are designed to take advantage of *XMM-Newton's* soft sensitivity. This method, combined with visual inspection of the SNR candidates in [S II] and Hα, yielded the discovery of three new SNRs in M33 (first reported in W15). As before, we first compute the HRs in these bands based on SNR spectra simulated in `XSPEC` with the model outlined above. The HRs computed from these simulated spectra are plotted with the same color-scheme as before in the top-right (N_H = 1×10^{20} cm^{-2}), bottom-left (N_H = 1.2×10^{21} cm^{-2}), and bottom-right (N_H = 3.5×10^{21} cm^{-2}) panels of Figure 8. The thick black arrow indicates the direction of increasing temperature (smaller to larger crosses). There is no clear distinction between abundance ratio values in these bands based on simulated spectra. The top-left panel of Figure 8 displays the HRs calculated from source counts in the above bands using BEHR (Park et al. 2006). Typical errors from BEHR for sources with 1000 counts, 300 counts, and 100 counts are displayed for reference. The points are again color-coded based on potential progenitor type from Jennings et al. (2014) or LL14. Similarly to the simulated data, there is no separation by progenitor type based on HRs in these bands.

3.5 X-ray Morphology: Power-Ratios

A basic question about an SNR is the nature of the supernova explosion. One way to tackle this question, as demonstrated by Lopez et al. (2009, 2011), is through the X-ray morphology of the SNR. Specifically, Lopez et al. (2009, 2011) showed that the X-ray morphologies of young, ejecta-dominated SNRs are correlated with SN progenitor type as determined from other methods, like spectral fits. Lopez et al. (2009, 2011) determined progenitor type (Type Ia versus CC) for a subsample of Milky Way and Magellenic Cloud SNRs through a multipole expansion of the X-ray surface brightness of each source. This method produces quantitative measurements of morphological asymmetry for SNRs, and is referred to as the "power-ratio" method. Lopez et al. (2009, 2011) find that for ejecta dominated SNRs, Type Ia SNe are "statistically more spherical and mirror symmetric" than CC SNe, particularly in the 0.5-2.1 keV band.

Because this method has thus far only been applied to relatively nearby SNRs, we have performed a series of tests on a subset of the Lopez et al. (2011) data to determine the spatial resolution and number of counts necessary for determining SN progenitor type via the power-ratio method at distances greater than the Magellenic Clouds. To test the spatial resolution limits, we bin the data for a subsample of LMC SNRs sequentially until the resulting values change the quantitative morphologies. With each binning we re-calculate the SNR centroid based on the new image. We find that binning the data by four, eight, and sixteen and recalculating the power-ratios preserves the separation between the two types. Our tests reveal that the decreased spatial resolution at the distance of M33 should not affect our ability to type SNRs based on morphology as long as the SNRs possess enough counts. However, at high enough binning, it becomes apparent that there are too few pixels to extract robust morphological information. The results become significantly unreliable when all the counts are contained in less than roughly 100 pixels, depending on number of counts. Thus the maximum distance at which we can apply this technique depends on the size of the SNR as well as the distance. We find a limiting distance for this method of $\sim$ 1200 kpc for the 0.5" *Chandra* pixel size and the largest SNR radius in Lopez et al. (2011) (r $\sim$ 30 pc). Adopting more conservative radii for young, ejecta-dominated SNRs of 20 pc and 10 pc yields limiting distances of $\sim$ 830 kpc, and $\sim$ 410 kpc, respectively.

To test the count threshold, we take a random sampling of between 1 and 10% of the original counts from a sample of LMC SNRs keeping the images at full resolution and recalculating the power-ratios. We find that the method produces reliable results down to 2×10^3 counts for Type Ia and down to 3×10^2-4×10^2 counts for CC SNe. Below these count thresholds the method begins to produce unphysical results, i.e. power ratios with errors that include negative values. CC SNe are more robust to this effect because they initially have higher power ratios for both the octopole and quadrupole moments; SNRs that have lower power-ratios with larger error bars require more counts to get a robust typing. Therefore, we find that at least 2×10^3 counts are needed to robustly separate CC SNR progenitors from Type Ia SNR progenitors. Taken collectively, our tests demonstrate that SNRs with a radius of 20 pc and $\geq 2\times 10^3$ counts can have their progenitors typed via the power-ratio method out to the distance of M33. While there are a handful of SNRs in M33 with the requisite number of counts, none of these are large enough (r $>$ 20 pc) to utilize the power-ratio method for robust typing. We have verified this by testing the method on a few of the largest and brightest SNRs from the ChASeM33 survey and finding unphysical answers. In order to determine the quantitative morphologies of a large enough sample ($\sim$ 50) of SNRs in M33, our analysis suggests we would need an X-ray telescope with $\sim$ 0.03" resolution (17$\times$ the resolving power of *Chandra*), and with a 0.4 m^2 collecting area (10$\times$ the collecting area of *Chandra*).

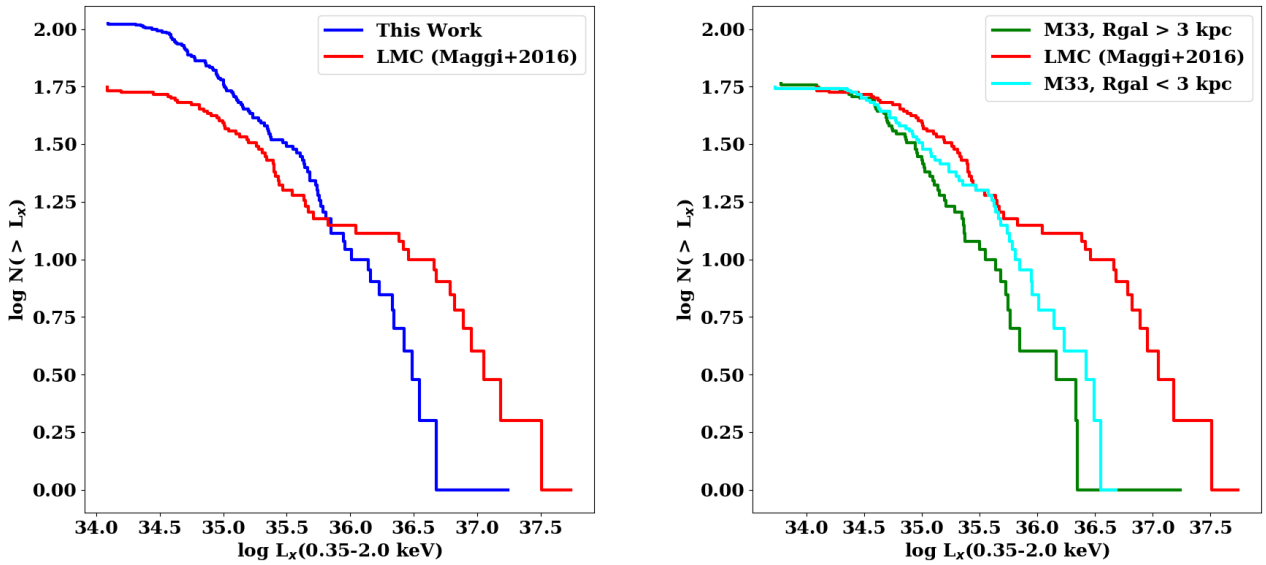

Figure 9. *Left*: Cumulative X-ray luminosity function (XLF) for all 3σ SNR detections from this work in blue. Cumulative XLF for the LMC from Maggi et al. (2016) in red. *Right*: Cumulative XLF for the inner 3 kpc of M33 (cyan, solar metallicity) and the outer 3 kpc (green, LMC-like metallicity) with the LMC XLF (red) for reference.

4 DISCUSSION

Our deep XMM-Newton survey of M33 complements the high spatial resolution of the SNR candidates measured by the ChASeM33 survey with increased counts for spectral fitting, expanded survey area, and increased soft sensitivity for SNR detection. In this section we explore the implications of our results for the SNR X-ray luminosity function, and the X-ray detectability of SNRs.

4.1 Supernova Remnant X-ray Luminosity Function

We first construct the X-ray luminosity function (XLF) in the 0.35-2.0 keV band for all detections in this work (3σ measurements) as shown in Figure 9. We overplot the XLF from Maggi et al. (2016) in red for comparison, transforming their 0.3-8.0 keV luminosities into the 0.35-2.0 keV band using WebPIMMS, and assuming an `apec` spectrum with kT=0.6 keV, M33 hydrogen column density of of 1×10^{21} cm^{-2}, and a galactic absorption component of 6×10^{20} cm^{-2}. This SNR catalog has 11 detections with $L_X > 10^{36}$ erg s^{-1}, as compared to 13 in the LMC, but fewer sources (three) at luminosities greater than $> 10^{36.5}$ erg s^{-1} than are found in the LMC (eight). The limiting luminosities for this survey and that of Maggi et al. (2016) are of the same magnitude: L_X(0.2-2.0 keV) = 7.2×10^{33} ergs s^{-1}, and L_X(0.3-8.0 keV) = 7.0×10^{33} ergs s^{-1}, respectively.

The shape of the LMC XLF, as discussed by Maggi et al. (2016) is clearly complex, and differs from the simple power-law distribution that can be used to describe the M33 XLF. At the faintest end, there are likely incompleteness effects for both catalogs, but such claims cannot be made at the bright end, thus necessitating an explanation of the discrepancies for the population of bright SNRs. We discuss several possible explanation below.

The explanation is unlikely to be the current star formation rate (SFR). The SFRs of the two galaxies are similar: between 0.2–0.4 $M_\odot$ yr^{-1} in the LMC over the last 100 Myr, with an increase to a rate of 0.4 $M_\odot$ yr^{-1} occurring in the last 12 Myr (Harris & Zaritsky 2009), and an average rate of 0.3 $M_\odot$ yr^{-1} in M33 over the last 100 Myr (Williams et al. 2013). Given these SFRs, both galaxies would be assumed to have close to the same rate of CC SNe production.

Another possible explanation, as discussed by Maggi et al. (2016) is metallicity effects. In particular, a lower metallicity environment will host stars with weaker line-driven stellar winds. The consequence is smaller wind-blown cavities for massive stars such that the SN explosion is running into a dense shell of material earlier in its evolution, leading to brighter SNRs at earlier times (Dwarkadas 2005). It is clear that the LMC has more SNRs at the bright end than M33, but to test whether this is solely a metallicity effect with respect to M33 one needs to take into account the metallicity gradient in M33. To do so we construct the XLF for SNRs in M33 that are within 3 kpc of the galactic center, and the XLF for SNRs that are at galactocentric radii larger than 3 kpc, as the metallicity in M33 goes from near-solar values within 3 kpc to LMC-like metallicity outside 3 kpc (Magrini et al. 2007). The two M33 XLFs are depicted in the right-hand panel of Figure 9. In M33 the SNRs at higher metallicity (< 3 kpc, cyan curve) have higher luminosities than those at lower metallicity (> 3 kpc, green curve), which is exactly the opposite of the expected behavior if the luminosity differences are due to differences in progenitor wind mass-loss rates alone. If metallicity was the primary driver of differences in the SNR XLF one might expect the SMC, as the lowest metallicity galaxy, to host even more SNRs at the bright end than the LMC. As noted in Maggi et al. (2016) this is not the case. Furthermore, at later times the effects of SNe exploding into environments of differing densities would be largely erased, so metallicity effects on the surrounding medium would only be distinguishable for a younger population of SNRs.

Maggi et al. (2016) also found that SN type and ISM structure did not seem to play a strong role in the SNR XLF shape in the LMC. The ratio of Type Ia versus CC SNRs in the XLF is difficult to compare across galaxies, as we do not have a definitive set of SN types for a large sample of M33 SNRs; however, both galaxies are likely dominated by core-collapse events. Maggi et al. (2016) note that the ratio of CC to Type Ia SNRs is slightly higher at the bright end of the LMC XLF, but not strongly so. Furthermore, while

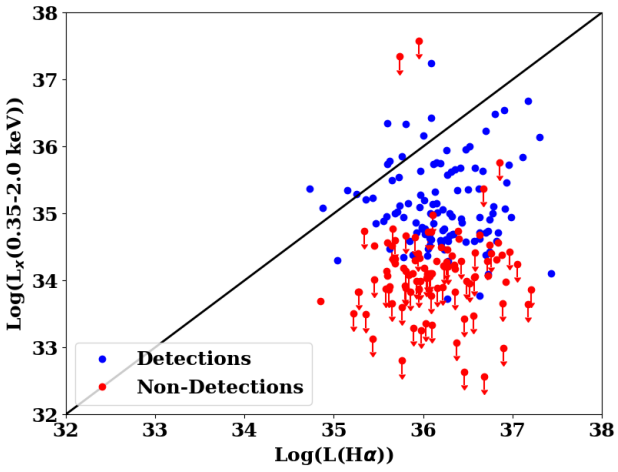

Figure 10. Comparison between the luminosities in 0.35-2.0 keV band from this work and the Hα luminosities from LL14. Red circles are SNR candidates non-detected in X-rays, and blue circles are SNRs detected at the 3σ level in X-rays. Sources that lie to the left and above the black diagonal line have X-ray luminosities greater than their Hα luminosities.

differences in the SNR brightness distribution could also arise from SNe that are exploding into non-uniform interstellar medium, Maggi et al. (2016) found no significant spatial correlation between SNRs in different luminosity bins and HI maps of the LMC. However, HI maps may be an imperfect indicator of "local" density around an SNR, so we cannot fully rule out that local density variations in the vicinity of SNRs contribute to different SNR luminosity distributions. In fact, one may even expect a more uniform ISM in a large, spiral galaxy like M33, as compared to LMC, which would result in SNRs with lower X-ray luminosities in an M33-like galaxy.

Finally, it may be that the most plausible explanation for the differences in SNR XLF shapes is that the star formation histories (SFHs) are different on a 50 Myr timescale, which would be relevant for SNe production. The total LMC SFR has increased by a factor of 2 over the past 50 Myr (Harris & Zaritsky 2009) which could result in a top-heavy progenitor mass distribution compared with a constant SFR. For example, SN1987A had a relatively massive progenitor (20 M$\odot$; Woosley et al. (1988)). We do not possess a global and resolved star formation history for M33, but based on the SNR progenitor mass distribution in M33 with peak mass at around 8 M$_\odot$ from Jennings et al. (2014) it is likely that M33 has a near constant SFR on this timescale. Furthermore, M33 is relatively high-mass and isolated compared to the LMC, making it less likely to change its global SFR significantly on timescales as short as 50 Myr. Thus, it is possible that differences in the XLF distributions at the bright end between the LMC and M33 are due the progenitor mass distributions leading to more bright, young SNRs in the LMC than in M33.

4.2 Detectability

The M33 XLF appears to flatten around 3×10^{34} erg s^{-1}, implying that our sample may still be incomplete at the faintest luminosities, and that with increased sensitivity the entire SNR population of M33 could be detected. To explore X-ray detectability we first compare the luminosities in the 0.35-2.0 keV band for all sources to the Hα luminosities from LL14. In Figure 10 we plot the X-ray luminosity in this band versus the Hα luminosity and find no significant correlation between the luminosities for either X-ray detections (blue points) or X-ray non-detections (red points, sources from the optical catalogs that were measured at the 2σ or upper-limit level in X-rays). Similarly to L10, we find that only one SNR has an X-ray luminosity significantly higher than its Hα luminosity (i.e. falls above the black line), and this is the brightest SNR in the sample, XMM-041 (L10-025). While it does appear that SNRs that are brighter at X-ray wavelengths also have generally higher Hα luminosities, there is a large spread in the X-ray to Hα luminosity comparison. The lack of strong correlation between luminosities can be explained by differences in the regions of the SNR being probed by each diagnostic. Namely, the X-ray luminosity is probing the region of the reverse shock, which is generally a region of higher temperature that cools more slowly. The Hα luminosity, by contrast, originates from recombination in the cooler, more dense shell region, which tends to cool on shorter timescales (Long et al. 2010; Leonidaki et al. 2013). The lack of correlation may also be due to the presence of non-uniform ISM, rather than regions of differing temperatures (Pannuti et al. 2007).

We also compare the cumulative size distribution for all X-ray detected SNRs versus all sources (detections and candidates) in our catalog with D < 50 pc to look for differences between the slopes of the distributions of each population. We choose this size cutoff, because the population of SNRs and SNR candidates is not complete above D ~ 50 pc. Our results are plotted in Figure 11 both for sizes from LL14 (left panel) and sizes from L10 (right panel). We find that the addition of 2σ and upper-limit measurements to the cumulative distribution tends to steepen the slope. This is likely because the population of SNR candidates non-detected in X-rays are biased towards larger diameter sources, as can also be seen in Figure 12. Likewise the slope of the cumulative distribution when using the LL14 sizes is steeper than the slope when using only L10 sizes, owing to the fact that the LL14 radii are systematically larger than those measured by L10. The slopes of the cumulative distributions for the 3σ SNR detections only are $\alpha \sim 2.5$ and $\alpha \sim 2.3$ when using LL14 and L10 size measurements, respectively. Both measured slopes are consistent with $\alpha = 2.5$, which is the slope expected for a population of SNRs in the Sedov phase. However, there are also various selection effects that can lead to biases in the sample of SNRs in a cumulative size distribution. For example, ISM conditions can strongly affect both the size and luminosity evolution of an SNR, though without detailed constraints on local ISM conditions we are unable to quantify the impact of such an effect. Surveys such as this one that confirm SNR candidates primarily on the basis of both optical and thermal X-ray emission are also liable to miss some young, X-ray emitting SNRs, thus biasing an optically selected and X-ray confirmed sample towards larger diameter SNRs.

In addition to the cumulative size distribution of the sample, we also look at the overall size distribution of all detections versus non-detections at all diameters. We plot this distribution in Figure 12, with all sources at D > 100 pc placed in the rightmost bin. The X-ray detected SNR sample extends to smaller diameters, implying that most small diameter SNRs are detected in X-rays. By contrast, the X-ray non-detections display a bias towards larger sizes, and have a sharper cutoff at smaller diameters than the population of sources detected in X-rays. The difference in diameters between the X-ray detected and X-ray non-detected sample may be attributed to age, or evolutionary effects, as young SNRs in the free expansion phase are likely to display X-ray emission, while older SNRs in the radiative phase show stronger optical emission (e.g. Leonidaki et al. 2010). This difference in sizes between the two populations leads to

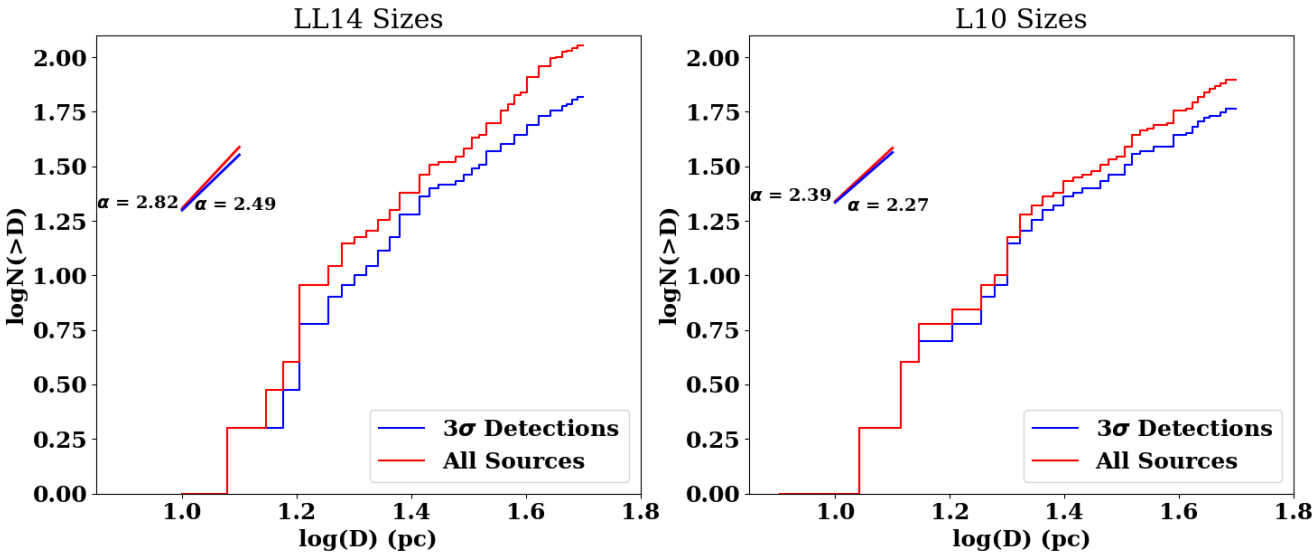

Figure 11. Cumulative size distribution for all 3σ detections (blue) versus all candidates (red) with D < 50 pc in the sample for sizes measured by LL14 (left panel) and sizes measured by L10 (right panel). We measure slopes of $\alpha \sim 2.8$ and $\alpha \sim 2.5$ for all sources and all detections, respectively, using LL14 sizes. We find slopes of $\alpha \sim 2.4$ and $\alpha \sim 2.3$ for all sources and all detections, respectively, using L10 sizes. The slopes for all detections are in good agreement with the slope of $\alpha = 2.5$ expected of a population of SNRs in the Sedov phase.

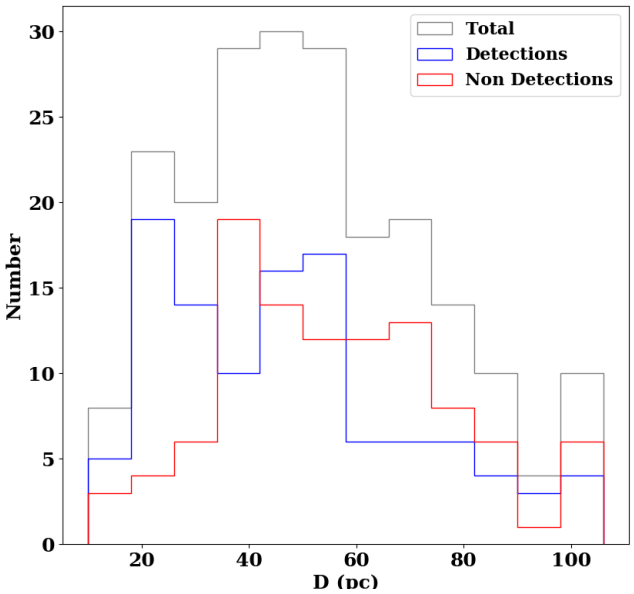

Figure 12. Histogram of sizes from L10 and LL14 for all non-detections (red) and detections (blue) in this sample. All sources with D> 100 pc are put into the rightmost bin.

a steepening of the slope of the cumulative distribution when SNR candidates that are non-detected in X-rays are included.

Finally, we compare the distribution of [SII]/Hα ratios for SNRs detected in X-rays versus those candidates undetected in X-rays in this catalog. The [SII]/Hα ratio is typically used as a way to distinguish optical emission from shocked regions in SNRs from emission from HII regions, with a cutoff at > 0.4 for classification as an SNR candidate. Higher [SII]/Hα values are indicative of regions with radiative shocks where enough recombination has occurred to produce significant [SII] emission, as in SNRs. In Figure 13 we demonstrate that there are two distinct populations in the [SII]/Hα distribution, with the SNR candidates non-detected in X-rays being drawn from a distribution with on average lower measured [SII]/Hα than the population of X-ray detected SNRs. To determine if these populations are physically distinct, we look for correlations between [SII]/Hα and object size and surface brightness as shown in the bottom two panels of Figure 13. We find no strong correlation between [SII]/Hα ratio and object size, and only a slight correlation between surface brightness and this ratio, with the lower surface brightness non-detections displaying on average higher [SII]/Hα values (bottom-left panel of Figure 13). It is possible that some of the X-ray non-detections at low [SII]/Hα (but above the 0.4 SNR candidate threshold) could represent the tail-end of a log-normal error distribution of line ratios of ionized nebulae. An example of such a distribution containing ~ 480 sources with a mean [SII]/Hα value of 0.1 and $\sigma \sim 0.1$ is over plotted in red on the top-right panel of Figure 13.

The application of the cutoff at [SII]/H$\alpha \sim 0.4$ for optically identifying SNR candidates should not be discounted based on a number of X-ray non-detected SNR candidates that also fall above this threshold, as this may be due to differences in varying shock conditions, or circumstellar environment on small scales. For example, SNRs that have not encountered enough dense material may not form radiative shocks, and would therefore not display high [SII]/Hα values. Similarly, if the metallicity of the ISM is non-uniform one might expect different distributions of [SII]/Hα depending on location in the galaxy. To test for environmental differences we construct a histogram of the galactocentric radii for all X-ray detected SNRs (blue) and X-ray non-detected SNR candidates (red) in Figure 14. The population of X-ray detections (sources with higher [SII]/Hα, as can be seen from the upper left plot of Figure 13) are located at preferentially smaller galactocentric distances than the population

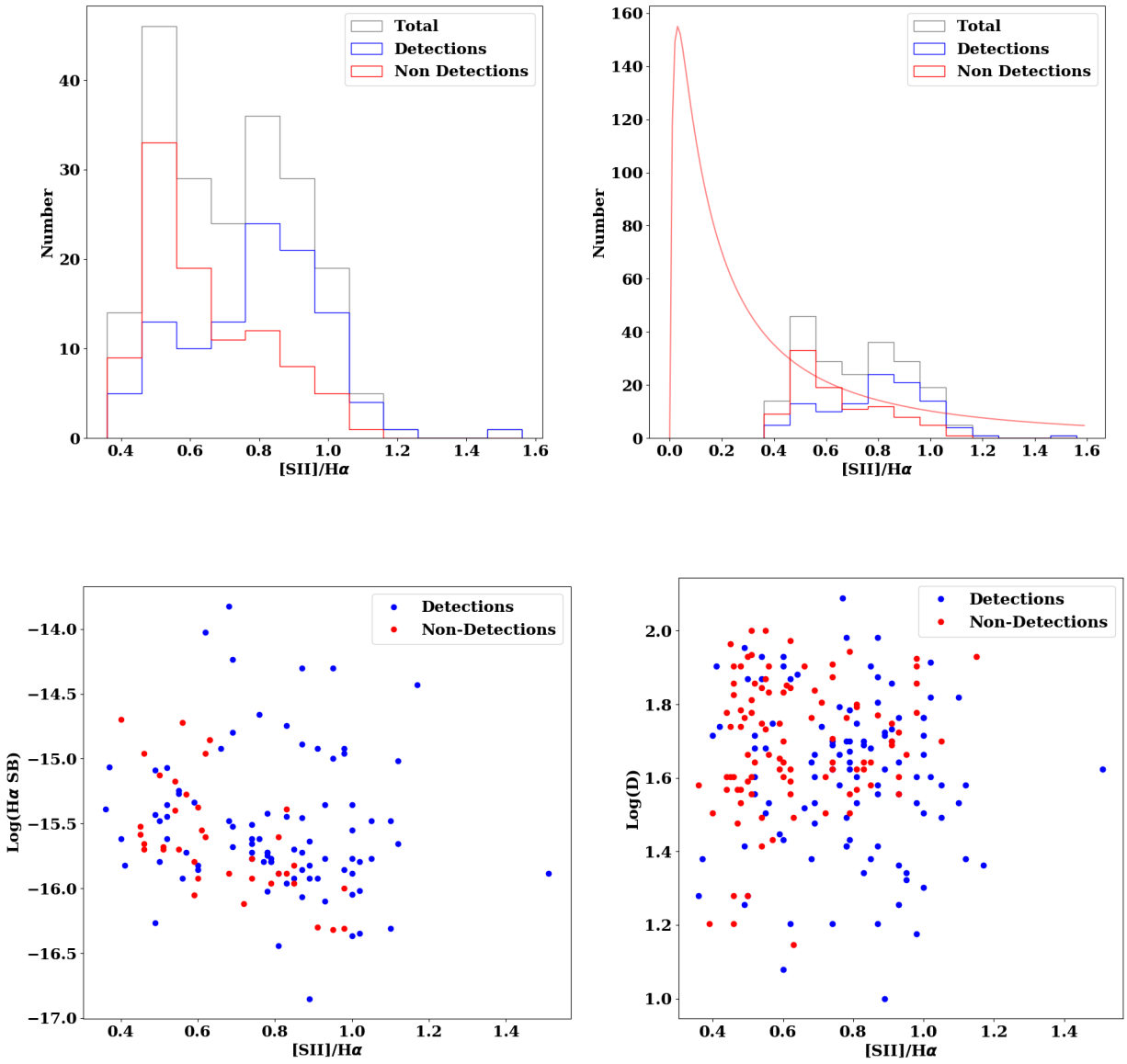

Figure 13. *Top left*: Histogram of [SII]/Hα ratios from L10 and LL14 for all SNR candidates non-detected in X-rays (red) versus X-ray detected SNRs (blue) in the sample. *Top right*: A log-normal error distribution of line ratios with a mean of 0.1 and σ value of 0.1 overplotted with respect to the population of X-ray non-detections. *Bottom left*: [SII]/Hα ratios from L10 and LL14 for all SNR candidates non-detected in X-rays (red) versus X-ray detected SNRs (blue) versus the measured Hα surface brightness values from L10. *Bottom right*: [SII]/Hα ratios from L10 and LL14 for all SNR candidates non-detected in X-rays (red) versus X-ray detected SNRs (blue) versus SNR diameters in pc.

non-detected in X-rays (sources with lower [SII]/Hα). We find no evidence that this separation is due to a gradient in exposure time or detector location in the observations. Instead, the separation may point to a metallicity effect, as there is a known chemical abundance gradient in M33, with the highest metallicities occurring at galaxy center and decreasing outwards (Magrini et al. 2007; Neugent & Massey 2014). In particular, (Magrini et al. 2007) measure this gradient as comprised of two slopes with the break occurring at R $\sim$ 3 kpc, similar to the radius at which we see the separation between the two histograms in Figure 14. Alternatively, this separation could be due to the effects of differing densities, with higher densities in the inner parts of the galaxy leading to stronger X-ray emission, and high [SII]/Hα values.

5 CONCLUSIONS

We have carried out a deep *XMM-Newton* Survey of M33 to complement the one performed by *Chandra*. With the power of both datasets we have detected at 3σ confidence $\approx$ 50% of the SNR candidates in M33 from previous X-ray and optical surveys (e.g. L10, LL14). These 105 sources are all robust SNR detections verified by both optical and X-ray measurements. We performed detailed

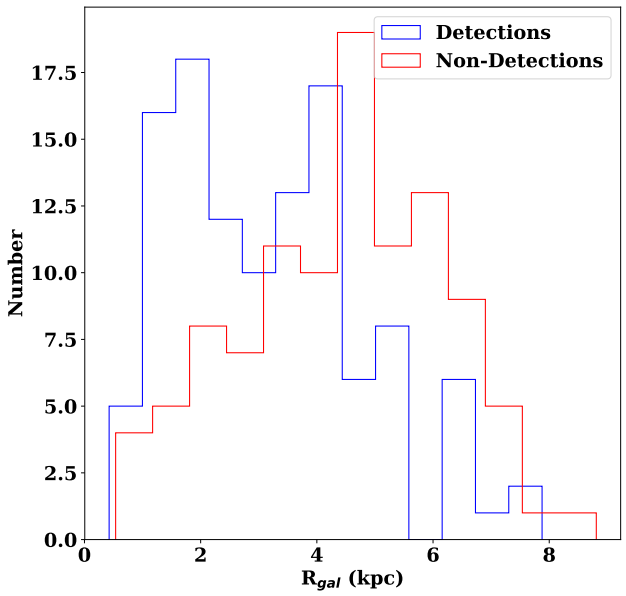

Figure 14. Histogram of galactocentric radii for all X-ray non-detections (red) and X-ray detections (blue) in this sample.

spectral fitting for 15 SNRs, twice the number possible than with the *Chandra* data alone. We find evidence of elevated O/Fe values from X-ray spectral fits for one SNR (XMM-068), implying that this SNR exploded in a region generally enriched by CC ejecta. Based on the fitted spectral parameters we also determine that the majority of the brightest SNRs are old (t > 1000 yrs), ISM-dominated SNRs.

To complement the spectral fitting analysis we have also tested the ability to type SNRs based on HRs in custom energy bands and X-ray morphology. We conclude that HRs or colors alone are too coarse as methods for detailed typing due to uncertainties in HRs coupled with degeneracies between the lines contributing to specific energy bands, SNR temperatures, and absorption values. In addition, due to current limits on telescope collecting area and resolving power we are unable to distinguish the SN progenitor type for a large sample of SNRs in M33 using quantitative morphology. However, the combination of quantitative morphology with HRs for SNRs in the much nearer Magellenic Clouds yields promising results for typing extragalactic SNRs independent of detailed spectral analysis for all SNRs in a sample.

We also use our large sample of SNRs to construct an XLF in both the inner (< 3 kpc, solar-like metallicity), and outer (> 3kpc, LMC-like metallicity) portions of M33 to test for metallicity effects on the luminosity distribution of the SNR population. In comparing XLFs in the inner and outer regions to one another, and also to the LMC SNR XLF, we find that while metallicity may play a role in SNR population characteristics, differing star formation histories on short timescales, and small-scale environmental effects appear to cause more significant differences between X-ray luminosity distributions.

Finally, we perform an analysis of the X-ray detectability of the M33 SNRs based on their physical properties. We compare this X-ray detected population of SNRs to the population of SNR candidates for which we have 2σ or upper-limit measurements in X-rays. The latter population is larger in diameter, located at preferentially larger galactocentric radii, and has lower measured [SII]/Hα values than the former. These differences suggest that the X-ray non-detected SNRs are likely comprised of a mixture of larger and/or fainter SNRs that potentially exploded into less dense, lower metallicity mediums that fall below our detection threshold, and some photoionized regions (HII regions or regions of diffuse ionized gas) whose measurement errors in the optical place them above the [SII]/Hα ratio cut used by most surveys. If we include only the X-ray detected SNRs in the cumulative size distribution, the distribution has a slope of 2.5, in accordance with a population of SNRs in the Sedov phase of evolution.

Future work will expand upon this large sample of well-characterized SNRs by exploring in more detail the interplay between host galaxy environmental factors and the resulting SNR properties. In particular, a more systematic study of surrounding ISM properties, coupled with resolved star formation histories in the vicinities of M33 SNRs will further quantify the dominant drivers behind SNR detectability, and add to the sample of SNRs with determined progenitor types.

Support for this work was provided by NASA grants NNX12AD42G and NNX12AI52G. T.J.G. and P.P.P. acknowledge support under NASA contract NAS8-03060 with the Chandra X-ray Center. We thank the referee for their very helpful comments in improving the manuscript.

REFERENCES

Badenes C., Bravo E., Borkowski K. J., Domínguez I., 2003, ApJ, 593, 358
Badenes C., Hughes J. P., Bravo E., Langer N., 2007, ApJ, 662, 472
Badenes C., Maoz D., Draine B. T., 2010, MNRAS, 407, 1301
Blair W. P., Kirshner R. P., Chevalier R. A., 1981, ApJ, 247, 879
Blair W. P., Winkler P. F., Long K. S., 2012, ApJS, 203, 8
Borkowski K. J., Lyerly W. J., Reynolds S. P., 2001, ApJ, 548, 820
Braun R., Walterbos R. A. M., 1993, A&AS, 98, 327
Chu Y.-H., Kennicutt Jr. R. C., 1988, AJ, 96, 1874
Dodorico S., Dopita M. A., Benvenuti P., 1980, A&AS, 40, 67
Dwarkadas V. V., 2005, ApJ, 630, 892
Freedman W. L., et al., 2001, The Astrophysical Journal, 553, 47
Gaetz T. J., et al., 2007, ApJ, 663, 234
Ghavamian P., Blair W. P., Sankrit R., Raymond J. C., Hughes J. P., 2007, ApJ, 664, 304
Gordon S. M., Kirshner R. P., Long K. S., Blair W. P., Duric N., Smith R. C., 1998, ApJS, 117, 89
Gordon S. M., Duric N., Kirshner R. P., Goss W. M., Viallefond F., 1999, ApJS, 120, 247
Green D. A., 2014, Bulletin of the Astronomical Society of India, 42, 47
Harris J., Zaritsky D., 2009, AJ, 138, 1243
Hughes J. P., et al., 1995, ApJ, 444, L81
Hughes J. P., Hayashi I., Koyama K., 1998, ApJ, 505, 732
Jennings Z. G., Williams B. F., Murphy J. W., Dalcanton J. J., Gilbert K. M., Dolphin A. E., Fouesneau M., Weisz D. R., 2012, ApJ, 761, 26
Jennings Z. G., Williams B. F., Murphy J. W., Dalcanton J. J., Gilbert K. M., Dolphin A. E., Weisz D. R., Fouesneau M., 2014, ApJ, 795, 170
Lacey C. K., Duric N., 2001, ApJ, 560, 719
Lee J. H., Lee M. G., 2014a, ApJ, 786, 130
Lee J. H., Lee M. G., 2014b, ApJ, 793, 134
Leonidaki I., Zezas A., Boumis P., 2010, ApJ, 725, 842
Leonidaki I., Boumis P., Zezas A., 2013, MNRAS, 429, 189
Long K. S., Helfand D. J., 1979, ApJ, 234, L77
Long K. S., et al., 2010, ApJS, 187, 495
Long K. S., Kuntz K. D., Blair W. P., Godfrey L., Plucinsky P. P., Soria R., Stockdale C., Winkler P. F., 2014, ApJS, 212, 21
Lopez L. A., Ramirez-Ruiz E., Badenes C., Huppenkothen D., Jeltema T. E., Pooley D. A., 2009, ApJ, 706, L106

Lopez L. A., Ramirez-Ruiz E., Huppenkothen D., Badenes C., Pooley D. A., 2011, ApJ, 732, 114
Maggi P., et al., 2014, A&A, 561, A76
Maggi P., et al., 2016, A&A, 585, A162
Magnier E. A., Prins S., van Paradijs J., Lewin W. H. G., Supper R., Hasinger G., Pietsch W., Truemper J., 1995, A&AS, 114, 215
Magrini L., Vílchez J. M., Mampaso A., Corradi R. L. M., Leisy P., 2007, A&A, 470, 865
Mannucci F., Della Valle M., Panagia N., Cappellaro E., Cresci G., Maiolino R., Petrosian A., Turatto M., 2005, A&A, 433, 807
Massey P., Olsen K. A. G., Hodge P. W., Strong S. B., Jacoby G. H., Schlingman W., Smith R. C., 2006, AJ, 131, 2478
Mathewson D. S., Clarke J. N., 1973, ApJ, 180, 725
Mathewson D. S., Ford V. L., Dopita M. A., Tuohy I. R., Long K. S., Helfand D. J., 1983, ApJS, 51, 345
Matonick D. M., Fesen R. A., 1997, ApJS, 112, 49
Milne D. K., 1979, Australian Journal of Physics, 32, 83
Neugent K. F., Massey P., 2014, ApJ, 789, 10
Pannuti T. G., Duric N., Lacey C. K., Ferguson A. M. N., Magnor M. A., Mendelowitz C., 2002, ApJ, 565, 966
Pannuti T. G., Schlegel E. M., Lacey C. K., 2007, AJ, 133, 1361
Pannuti T. G., Rho J., Heinke C. O., Moffitt W. P., 2014, AJ, 147, 55
Park T., Kashyap V. L., Siemiginowska A., van Dyk D. A., Zezas A., Heinke C., Wargelin B. J., 2006, ApJ, 652, 610
Pietsch W., Misanovic Z., Haberl F., Hatzidimitriou D., Ehle M., Trinchieri G., 2004, A&A, 426, 11
Raymond J. C., 1984, ARA&A, 22, 75
Reynolds S. P., 2008, ARA&A, 46, 89
Sabbadin F., 1979, A&A, 80, 212
Sarbadhicary S. K., Badenes C., Chomiuk L., Caprioli D., Huizenga D., 2017, MNRAS, 464, 2326
Sasaki M., Pietsch W., Haberl F., Hatzidimitriou D., Stiele H., Williams B., Kong A., Kolb U., 2012, A&A, 544, A144
Stark A. A., Gammie C. F., Wilson R. W., Bally J., Linke R. A., Heiles C., Hurwitz M., 1992, ApJS, 79, 77
Tüllmann R., et al., 2011, ApJS, 193, 31
Tuohy I. R., Dopita M. A., Mathewson D. S., Long K. S., Helfand D. J., 1982, ApJ, 261, 473
Vink J., 2012, A&ARv, 20, 49
Vink J., Laming J. M., Gu M. F., Rasmussen A., Kaastra J. S., 2003, ApJ, 587, L31
Williams B. F., Dalcanton J. J., Stilp A., Dolphin A., Skillman E. D., Radburn-Smith D., 2013, ApJ, 765, 120
Williams B. F., et al., 2015, ApJS, 218, 9
Wilms J., Allen A., McCray R., 2000, ApJ, 542, 914
Woltjer L., 1972, ARA&A, 10, 129
Woosley S. E., Pinto P. A., Ensman L., 1988, ApJ, 324, 466
Yamaguchi H., et al., 2014, ApJ, 785, L27
Zaritsky D., Elston R., Hill J. M., 1989, AJ, 97, 97

APPENDIX A: SPECTRAL EXTRACTION TECHNIQUES

The primary tool for spectral extraction is the `SAS` task *evselect*. One can use the selection expression of this task to define the location, in image coordinates, where the extraction should take place. The nature of this survey allows for a particular source to be found in different combinations of instruments and fields of data. FITS images were created with World Coordinate Systems for each of the 30 brightest sources. Background regions were selected manually using criteria recommended by the *XMM-Newton* Calibration Technical Notes. For the EPIC-MOS instruments, either an annulus around the source or a separate location that has an equivalent off-axis angle, related to the vignetting, and on the same CCD should be used. For EPIC-pn, the background extraction region should not be an annulus due to the possibility of out-of-time (OOT) events interfering. Backgrounds should instead be taken on the same CCD if possible and at an equivalent readout distance on the CCD (the same RAWY value). Selecting the background manually also allowed for the best possible location to be chosen, maximizing the value of the spectra. Through examination of spectra using three differently sized background regions–same extraction area as source, double the area, and ten times the area–we determined the optimal background size to use was double the area of the source region. Any larger and surrounding sources would make finding a source-free background difficult while trying to adhere to the suggested parameters. Using a simple script, these paired region locations were saved to text files in their observations specific image coordinates.

The *evselect* selection expressions, along with some parameter values like bin size and maximum channel, vary between the MOS and pn instruments. Depending on the instrument, the proper image coordinates for the source were fed to *evselect* and then repeated with the background region detector coordinates. The source and background extraction regions of the spectra were computed, followed by the generation of the redistribution matrix file (RMF) and ancillary response file (ARF). The RMF and ARF file names were written to the RESPFILE and ANCRFILE header keywords of both the source and background spectra using the `HEASARC FTOOLS` software task *grphha*.

If a source lay within the field of view of the PMH 47 observations (see W15 Section 2), we elected to combine those spectra using the `FTOOLS` software. Due to the varying roll angle of the PMH 47 observations, it was possible for a source to be out of the field of view or on a chip gap for one or more of the observations. This necessitated taking care to properly merge the header keywords, of which two were critical. The EXPOSURE keyword is simply summed, but the BACKSCAL keyword, which provides the number of sky pixels in the extraction area of the source was dealt with more carefully when the effective area (ARF) and response matrix (RMF) files from the different observations were combined. In particular, the BACKSCAL values(B_i) were weighted by the exposure time (E_i) in the manner of Huenemoerder, Davis, Houck and Nowak (2011).

$$B_{final} = \frac{1}{E_{total}} \sum_i (B_i E_i)$$

The source and background spectra were merged two at a time using `mathpha` and without error propagation as we decided to perform the error propagation based on counts alone. The final merged product had the BACKSCAL and summed EXPOSURE keywords written to the header. The ARF and RMF files of each observation were first individually combined to create a response file using `mkarfrmf`, and were then weighted by exposure and merged together using `addrmf`. In order for the combined files to work correctly in `XSPEC`, two additional keywords, POISSERR and STAT ERR needed to be changed in the source and background spectral files. When combining the spectra, the `mathpha` task also created a STAT ERR column which was found to be too conservative. This column was deleted and the updated keywords allowed error propagation to be determined based on the counts alone.

This paper has been typeset from a TEX/LATEX file prepared by the author.